Die approbierte gedruckte Originalversion dieser Diplomarbeit ist an der TU Wien Bibliothek verfügbar
The approved original version of this thesis is available in print at TU Wien Bibliothek.

Diplomarbeit

Motion Detection in MRI Using Wireless Accelerometers and Beat Pilot Tone

ausgeführt zum Zwecke der Erlangung des akademischen Grades eines

Diplom-Ingenieurs

unter der Leitung von

Assoc.-Prof. Dipl.-Ing. Dr. Elmar Laistler

(Zentrum für Medizinische Physik und Biomedizinische Technik, Medizinische Universität Wien)

und

Ao.Univ.Prof. Dipl.-Ing. Dr.techn. Martin Gröschl

(Institut für Angewandte Physik, Technische Universität Wien)

eingereicht an der Technischen Universität Wien

Fakultät für Physik

von

Bastian Rapp

Matrikelnummer: 12024763

Wien, im August 2023

Bastian Rapp   Martin Gröschl

Die approbierte gedruckte Originalversion dieser Diplomarbeit ist an der TU Wien Bibliothek verfügbar
The approved original version of this thesis is available in print at TU Wien Bibliothek.
TU WIEN Bibliothek Your knowledge hub

TECHNISCHE
UNIVERSITÄT
WIEN

MEDICAL UNIVERSITY
OF VIENNA

Diploma Thesis

in the master's Degree

Biomedical Engineering

at the

Vienna University of Technology

Faculty of Physics

with collaboration of the High Field MR Center in the Center for Medical Physics and
Biomedical Engineering at Medical University of Vienna

Topic:

Motion Detection in MRI Using Wireless Accelerometers and Beat Pilot Tone

Author: Bastian Rapp, B.Sc.

Student ID: 12024763

Professor and examiner: Ao.Univ.Prof. Dipl.-Ing. Dr.techn. Martin Gröschl

Supervisor: Assoc.-Prof. Dipl.-Ing. Dr. Elmar Laistler

Date of submission: 23. August 2023

Vienna, August 2023

Bastian Rapp

Martin Gröschl

Ich habe zur Kenntnis genommen, dass ich zur Drucklegung meiner Arbeit unter der Bezeichnung

Diplomarbeit

nur mit Bewilligung der Prüfungskommission berechtigt bin.

Ich erkläre weiter an Eides statt, dass ich meine Diplomarbeit nach den anerkannten Grundsätzen für wissenschaftliche Abhandlungen selbstständig ausgeführt habe und alle verwendeten Hilfsmittel, insbesondere die zugrunde gelegte Literatur, genannt habe.

Weiters erkläre ich, dass ich dieses Diplomarbeitsthema bisher weder im In- noch Ausland (einer Beurteilerin/einem Beurteiler zur Begutachtung) in irgendeiner Form als Prüfungsarbeit vorgelegt habe und dass diese Arbeit mit der vom Begutachter beurteilten Arbeit übereinstimmt.

Wien, im August 2023

Bastian Rapp

Die approbierte gedruckte Originalversion dieser Diplomarbeit ist an der TU Wien Bibliothek verfügbar
The approved original version of this thesis is available in print at TU Wien Bibliothek.
TU WIEN Bibliothek Your knowledge hub

Danksagung

Ein großes Dankeschön an erster Stelle gilt meinem Betreuer Elmar Laistler, der mich in jeder Hinsicht unterstützt hat, seine Expertise an vielen Stellen eingebracht hat und mit seiner großen Begeisterung für dieses Projekt vieles selbst voran gebracht hat. Generell danke ich dem ganzen Team des RF Labs, die eine super Arbeitsatmosphäre hergestellt haben und alle immer sehr hilfsbereit waren. Besonders Lena Nohava und Roberta Frass-Kriegl hatten immer ein offenes Ohr für mich, haben tatkräftig bei allen Messungen unterstützt und auch als Probandinnen fungiert. Auch Onisim Soanca ist hervorzuheben, der besonders am Anfang nicht müde wurde, meine fehlende Hardware-Kompetenz aufzubessern und mir jegliche Fragen zu beantworten. Viel Motivation habe ich auch durch Kommilitone und Freund Ernesto Gomez-Tamm bekommen, der mit mir parallel geschrieben hat und wir uns gegenseitig immer unterstützen konnten.

Ebenso möchte ich mich bei Prof. Badurek bedanken und beste Genesungswünsche schicken, der trotz schwerer Erkrankung für uns noch alles organisiert hat. In diesem Zuge dann vielen Dank an Prof. Gröschl, der sehr kurzfristig als betreuender Professor für Prof. Badurek eingesprungen ist.

Ein genereller Dank geht an meine Familie, die mich in meinem Bestreben zu studieren und den Master in Wien zu machen immer unterstützt haben und mir in vielerlei Hinsicht den Rücken freigehalten haben.

Die approbierte gedruckte Originalversion dieser Diplomarbeit ist an der TU Wien Bibliothek verfügbar
The approved original version of this thesis is available in print at TU Wien Bibliothek.
TU WIEN Bibliothek Your knowledge hub

Kurzfassung

Magnetresonanztomographie (MRT) ist ein etabliertes medizinisches Bildgebungsverfahren, das nicht invasiv ist, einen hohen Weichteilkontrast aufweist und auf der Wechselwirkung von Kernspins mit externen Magnetfeldern beruht. MRT-Messungen im Brustbereich mit speziellen Brustspulen sind eine aktuell erforschte Anwendung dieser Technik, die die Mammographie bei der Diagnose von Brustkrebs ersetzen soll. Aufgrund der langen Scanzeiten werden MRT-Messungen im Allgemeinen und besonders bei der Anwendung im Brustbereich stark durch Bewegungsartefakte beeinträchtigt, die z. B. durch die Atembewegungen der Patienten entstehen können und die Bildqualität einschränken.

In dieser Diplomarbeit werden Möglichkeiten untersucht, die Bewegung des Patienten bei Messungen mit einer tragbaren und flexiblen Brustspule zu erfassen, um diese Daten zur Bewegungskorrektur der resultierenden Bilder zu nutzen. Mit einem Setup des kürzlich entwickelten Beat-Pilot-Tone (BPT) Verfahrens, bei dem externe Hochfrequenz-Signale von den MR-Empfangsspulen aufgenommen werden und die Amplitudenmodulation mit der Patientenbewegung korreliert, konnten erfolgreich und zuverlässig zeitaufgelöste Bewegungssignale parallel zur MR-Messung erzeugt werden. Dieser Aufbau ist für den klinischen Einsatz attraktiv, da keine zusätzliche Hardware auf der Spule benötigt wird und die Daten direkt in den Rohdaten des MR-Scanners enthalten sind. Der GRICS-Algorithmus (Generalized reconstruction by inversion of coupled systems) wurde in Kombination mit den aufgezeichneten bewegungskorrelierten Zeitverläufen zur Bewegungskorrektur der Bilder verwendet, und es konnte gezeigt werden, dass eine wesentliche Verbesserung der Bewegungsartefakte erreicht werden konnte. Dies motiviert die weitere Untersuchung und den potenziellen klinischen Einsatz dieses Systems.

Die approbierte gedruckte Originalversion dieser Diplomarbeit ist an der TU Wien Bibliothek verfügbar
The approved original version of this thesis is available in print at TU Wien Bibliothek.

Abstract

Magnetic resonance imaging (MRI) is an established medical imaging technique that is non-invasive, has high soft tissue contrast and relies on the interaction of nuclear spins with external magnetic fields. Free breathing supine breast MRI is an application of that technique with specific chest coils, that is currently researched and set to substitute mammography for the diagnosis of breast cancer. Due to the long scan times, MRI in general and in specific chest imaging is heavily affected by motion artefacts that arise for example from breathing motion of the patient.

This diploma thesis explores options to record the patient motion in measurements with a wearable and flexible chest coil, in order to use this data for motion correction of the resulting images. A setup of the recently proposed beat pilot-tone (BPT) technique, where external RF signals are picked up by the receiving MR coils and the amplitude modulation correlates with patient motion, was built and proved to produce reliable time-resolved motion signals. This setup is attractive to use clinically, since no additional on-coil hardware is needed and the data is directly accessible within the MR scanner’s raw data. The GRICS (Generalized reconstruction by inversion of coupled systems) algorithm was used in combination with the recorded motion-correlated time courses for motion correction of the images and it was shown that a substantial improvement of motion artefacts was achievable. This motivates the further investigation and potential clinical use of this setup.

Die approbierte gedruckte Originalversion dieser Diplomarbeit ist an der TU Wien Bibliothek verfügbar
The approved original version of this thesis is available in print at TU Wien Bibliothek.
TU WIEN Bibliothek Your knowledge hub

Table of contents

Die approbierte gedruckte Originalversion dieser Diplomarbeit ist an der TU Wien Bibliothek verfügbar
The approved original version of this thesis is available in print at TU Wien Bibliothek.

Die approbierte gedruckte Originalversion dieser Diplomarbeit ist an der TU Wien Bibliothek verfügbar
The approved original version of this thesis is available in print at TU Wien Bibliothek.

1 Introduction

Magnetic Resonance Imaging (MRI), a form of medical imaging, has become a popular and potent diagnostic tool that can give anatomical and functional insights in a non-invasive way. It can provide exceptional soft tissue contrast, which is used for diagnoses of a wide range of illnesses and conditions. The mechanism is based on the physical phenomenon of nuclear magnetic resonance (NMR), where structure, dynamics and chemical composition of molecules can be measured by aligning their magnetic moments to a strong static magnetic field and applying radiofrequency pulses. In clinical MRI applications, the target nuclei for this procedure is mainly hydrogen, which exists in large quantities in the human body and can create contrast for most soft tissues when acquiring images.

Despite its impressive capabilities, some downsides of MRI still cause major problems to this day, for example motion artefacts that occur due to the long scan times impairing the image accuracy. [1] Subconscious physiological patient movements like breathing, conscious patient body movements and even internal physiological processes like heartbeat can all result in image artefacts like blurring, ghosting or distortions. This can limit the diagnostic utility of the images, especially in heavily affected areas like the chest. Since breast cancer is one of the most common types of cancer affecting women, the diagnosis and exact localization plays a major role in modern medicine, requiring fitting imaging modalities. Mammography has been considered the gold standard for this type of diagnosis for a long time, however recently there has been a push to include MRI methods for more accuracy. [2] Free breathing supine breast MRI is the target of a chest coil developed by the Radio Frequency Lab of the Center for Medical Physics and Biomedical Engineering, that enables a diagnosis of breast cancer that is more accurate and also more pleasant for the patient. [3] As this coil comes in the form of a wearable vest making the coils move with the chest motion of the patient, it suffers from the aforementioned motion related artefacts. This requires some kind of motion correction, which is the motivation for this thesis.

Correcting for patient motion and dealing with the motion artefacts has been a relevant topic of research for a long time now, and several different approaches can be identified ranging from the prevention of motion to post-processing methods with recorded motion profiles. The latter option was chosen for this project, since patient breathing and heartbeat can obviously not be avoided in the target region. Two techniques were tested, where the first one was a direct measurement using a motion sensor, and the second one was a recently proposed beat pilot-tone approach, using external signals interacting with the coils. The goal was to produce motion profiles synchronized with the measurement that are usable by a partnering

Die approbierte gedruckte Originalversion dieser Diplomarbeit ist an der TU Wien Bibliothek verfügbar
The approved original version of this thesis is available in print at TU Wien Bibliothek.
TU WIEN Bibliothek Your knowledge hub

research group to correct the images with their algorithm for free-breathing MRI reconstruction.

Die approbierte gedruckte Originalversion dieser Diplomarbeit ist an der TU Wien Bibliothek verfügbar
The approved original version of this thesis is available in print at TU Wien Bibliothek.

2 Theoretical Background

2.1 Basics of Magnetic Resonance Imaging

To give context to the topic in general and to the methodological challenges involved in motion acquisition, a short introduction to the principles of MRI is given in the following. This by no means covers every aspect, but should offer a good overview.

2.1.1 Physics behind MRI

The physics involved to comprehensively describe the imaging process involves a lot of complex quantum mechanics and a good in depth explanation can be found for example in [4] or [5]. Here only the essential concepts are explained briefly.

2.1.1.1 Response of nuclear spins to magnetic fields

The underlying physical principle behind MRI is the phenomenon of nuclear magnetic resonance (NMR), which was first shown experimentally by Isidor Isaac Rabi in the 1930s. Based on that work, Bloch et al. [6] and Purcell et al. [7] investigated NMR for solids and liquids around 10 years later, laying the foundation for the usage in order to image the water content for example of the human body and earning them a Nobel prize. As indicated by the name, NMR stems from the magnetic properties of nuclei, namely their nuclear spin $\vec{I}$, which is formed by the sum of intrinsic angular momentums (spins) of the protons and neutrons that make up that nucleus. This quantum number only takes discrete values based on the distribution of nucleons, following the laws of quantum mechanics. For an uneven amount of nucleons it is a half-integer and for an even amount an integer, since the proton and neutron both have spin ½ and up and down spins build pairs with no overall spin. Its magnitude can be calculated by

$$|\vec{I}| = \hbar\sqrt{I(I+1)} \tag{1}$$

and without loss of generality the projection on the quantization axis $I_z = m_z\hbar$ also takes discrete values, where $m_z = -I, ..., I-1, I$, giving $2I+1$ configurations. The hydrogen nucleus for example, which is the most commonly used nucleus for imaging, consisting only of one proton, has the nuclear spin values +½ and -½ . The nuclear spin leads to a magnetic moment of

$$\vec{\mu} = \gamma\vec{I} \tag{2}$$

where γ is the gyromagnetic ratio, which is a constant depending on the nucleus. For the case of a hydrogen nucleus, i.e. a proton it can be calculated approximately by $\gamma = e/2m_p$. Now when an external static magnetic field B_0 is applied, the initially

Die approbierte gedruckte Originalversion dieser Diplomarbeit ist an der TU Wien Bibliothek verfügbar
The approved original version of this thesis is available in print at TU Wien Bibliothek.

randomly orientated magnetic moments caused by the nuclear spins interact with that field according to

$$\frac{d\overrightarrow{\mu}}{dt} = \gamma\overrightarrow{\mu} \times \overrightarrow{B_0} \tag{3}$$

The spins align either parallel or antiparallel to the external field and like a gyroscope exposed to gravity, this leads to precession of the magnetic moment around the field direction, visualized in Figure 1a. The frequency of that precession is the so called Larmor frequency, and can be calculated by

$$\omega_0 = \gamma B_0 \tag{4}$$

It therefore varies with external field strength and gyromagnetic ratio, for the hydrogen atom in a clinical use case of 3T it for example amounts to 127.74 MHz. Energywise, the interaction of magnetic moment and external field leads to a splitting of energy levels based on the spin configuration, which is called the Zeeman effect. The energy levels are given by

$$E = -\mu B_0 = -\gamma m_z \hbar B_0 \tag{5}$$

and visualized in Figure 1b for a spin one-half system. A transition between the states is only allowed for neighboring levels, therefore only if $\Delta m = \pm 1$ and can be achieved by emission or absorption of a photon as indicated by the curly arrow in the figure. The frequency of this photon is exactly the above mentioned Larmor precession frequency, therefore the energy difference is $\Delta E = \hbar\omega_0$.

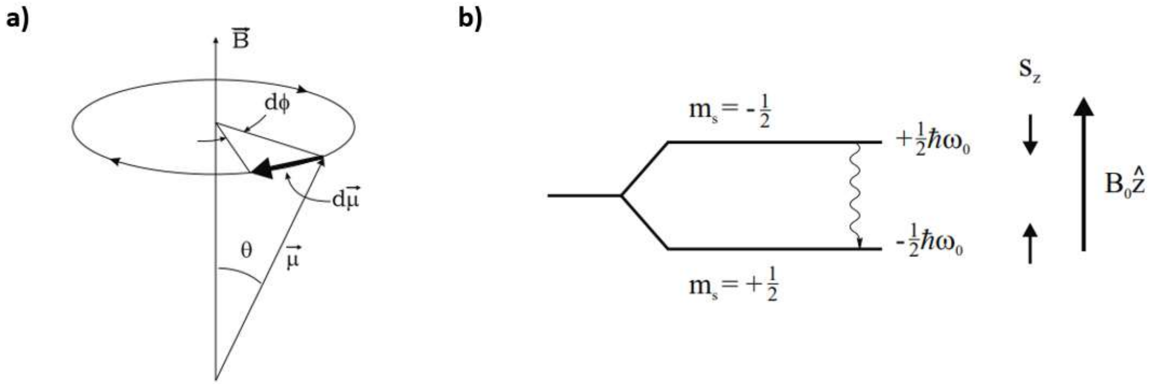

Figure 1: a) Precession of a magnetic moment around an external magnetic field **b)** Zeeman energy splitting of a spin one-half system while an external magnetic field is applied (reproduced from [4] with permission (license number: 5594280022150))

Die approbierte gedruckte Originalversion dieser Diplomarbeit ist an der TU Wien Bibliothek verfügbar
The approved original version of this thesis is available in print at TU Wien Bibliothek.

2.1.1.2 Magnetization and RF excitation

The explanations in the previous chapter show the behavior of one single nuclear spin in an external magnetic field, recall however that the main goal of MRI is to measure and image the proton density of macroscopic objects like body parts. Therefore the magnetization of large systems of spins is of interest. After applying the external field, the net longitudinal equilibrium magnetization of a system of spins corresponds to the population differences of the two energy levels coinciding with parallel and antiparallel alignment. Here the parallel alignment is the lower energy state following eq. 5 and therefore more populated in equilibrium. The population statistics follow the Boltzmann distribution, where in thermal equilibrium a nucleus has the probability

$$P_m = \frac{e^{-E_m/kT}}{\sum_m e^{-E_m/kT}} \tag{6}$$

of being in the state with energy E_m. Since the thermal energy at human body temperature is significantly higher than the quantum energy difference of the two states, the population difference at equilibrium is quite low, for example $(n_{1/2} - n_{-1/2})/n_{1/2} \approx \gamma\hbar B_0/kT \sim 10^{-5}$ at 1T [8]. Due to the high abundance of protons in tissue however there is still a measurable NMR signal.

To detect an electromagnetic signal proportional to the density of the target nuclei, an RF pulse is applied in order to induce transitions between the adjacent Zeeman levels described above. The pulse therefore has to have a frequency equal to the resonant Larmor frequency. This oscillating magnetic RF field B_1 rotates perpendicular to B_0 in the x-y-plane and eq. 3 can be adjusted to

$$\frac{d\vec{M}}{dt} = \gamma\vec{M} \times (\vec{B}_0 + \vec{B}_1) \tag{7}$$

where $\vec{M}$ is now the resulting magnetization including all magnetic moments. Effectively, the RF pulse tips the magnetization vector away from the z-axis, with the flip angle depending on the amplitude and duration of the pulse according to $\Delta\Theta = \gamma \int_0^t B_1(t)dt$. In practice, in many applications, this flip angle is 90° (π/2), so that the resulting magnetization vector is tilted into the transverse x-y-plane. This motion of the magnetic moments of the nuclei now induces an RF signal in nearby RF coils to form the MR image, where its intensity is dictated by the level of magnetization in the specific region. A visualization of this process can be seen in

Die approbierte gedruckte Originalversion dieser Diplomarbeit ist an der TU Wien Bibliothek verfügbar
The approved original version of this thesis is available in print at TU Wien Bibliothek.

figure 2. For different imaging requirements, multiple RF pulses can also be compiled into pulse sequences.

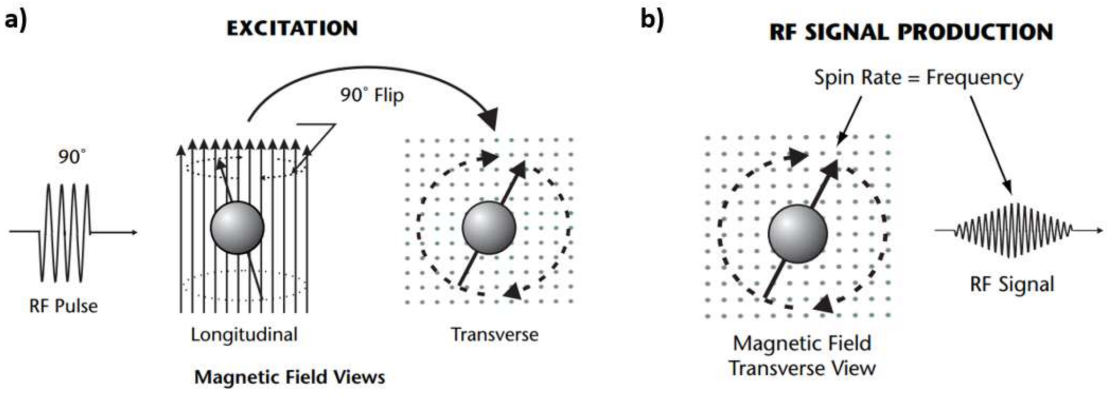

Figure 2: a) RF excitation and consequent 90° flipping of the magnetization vector into the transverse plane **b)** RF signal production via the resulting motion of the magnetization (reproduced from [9] with permission (license number: 5598710370840))

2.1.1.3 Relaxation and Bloch equations

After the RF excitation of the spins, the system seeks to return to the energetically more favorable equilibrium state, going back to alignment with B_0. This is called relaxation, and the involved two processes and their duration can be used for image formation. The first process is the longitudinal relaxation, being the exponential recovery of the original magnetization in z-direction; the associated time constant is called T_1. The process governing this is called spin-lattice relaxation and describes interactions of the single spins with their surrounding molecular lattice like thermal energy transfer. The rate of relaxation depends on factors like the strength of the magnetic field, the temperature and the properties of the surrounding lattice. The second process refers to the transverse relaxation, being the exponential decay of the magnetization in the x-y-plane, associated with the time constant T_2. This is governed by the so-called spin-spin relaxation, therefore describes interactions of the spins with each other. In an ideal system, identical non-interacting nuclei in a uniform static field would all have spins precessing at the exact same frequency in the transverse plane. In reality however, most nuclear spins precess with a slightly different frequency, due to field inhomogeneities or magnetic interactions between the nuclei. This leads to dephasing of the nuclear spins, resulting in the mentioned exponential decay of transverse magnetization. Crucial for imaging is now that different tissues have different relaxation times, which can be used to create contrast and make different anatomical structures visible. In T_1-weighted images for example, which can be achieved by choosing the right pulse sequence, fat with a short T_1

Die approbierte gedruckte Originalversion dieser Diplomarbeit ist an der TU Wien Bibliothek verfügbar
The approved original version of this thesis is available in print at TU Wien Bibliothek.

appears bright and fluids with a long T_1 appear dark. In T_2-weighted images the inverse is the case.

This behaviour of the magnetization including the relaxation processes is summed up in the following Bloch equations, for all three dimensions:

$$\frac{dM_z}{dt} = \frac{M_0 - M_z}{T_1} \tag{8}$$

$$\frac{dM_x}{dt} = \omega_0 M_y - \frac{M_x}{T_2} \tag{9}$$

$$\frac{dM_y}{dt} = -\omega_0 M_x - \frac{M_y}{T_2} \tag{10}$$

2.1.2 Imaging procedure

In the previous section an overview of the necessary physics to create a measurable RF signal from a sample via NMR was described, what is still missing however is how that signal can be used to create actual 2D or 3D images. A summary of that imaging procedure will be given in the following.

2.1.2.1 Positional encoding with gradients

In order to form an image, it is essential to be able to spatially discriminate the received RF signals from the samples after the excitation. In order to do that, the fact that after eq. 4 the Larmor frequency is dependent on the magnetic field strength is utilized and therefore the position can be encoded by frequency. Spatially changing the external field for example in z-direction then changes the frequency subsequently according to $\omega(z) = \gamma B(z)$. Now by applying an inverse fourier transform, the received frequency spectrum can be mapped onto a spatial dimension. In practice this is achieved by adding coils that create a linear gradient field in the respective direction, that is added to B_0. Generally in z-direction (parallel to B0), first during the excitation pulse a slice selection gradient G_z is applied, that varies the Larmor frequency in z-direction so that only a specific transversal body slice is selected. Then for the readout of that slice, another gradient in x-direction changes the frequency of the transverse precession with x, while one in y-direction changes the phase of precession with y. This means as a resulting signal an image matrix can be acquired, where every x-y-point is distinguished by frequency and phase. Figure 3

Die approbierte gedruckte Originalversion dieser Diplomarbeit ist an der TU Wien Bibliothek verfügbar
The approved original version of this thesis is available in print at TU Wien Bibliothek.
TU WIEN Bibliothek Your knowledge hub

shows a visualization of the gradient coil setup and a basic sequence to generate a signal.

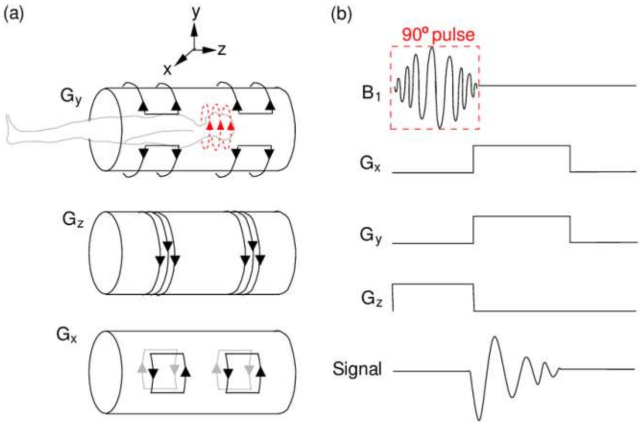

Figure 3: a) Gradient coil setup around the bore **b)** Imaging sequence with use of gradients to create one RF signal (reproduced from [10] with public permission)

2.1.2.2 k-space

The measured matrix is a collection of complex numbers that is called the k-space and can be converted to the image via fourier transform as mentioned above. One example of a slice of k-space of a brain measurement and the corresponding image after a fourier transform can be seen in figure 4. For the interpretation of the k-space image it has to be noted that the values here are a mathematical representation of spatial frequencies. Each position in k-space does not respond to a position in the image, however to a specific spatial frequency, with lower frequencies being in the k-space center. This fact can be used so that different parts of the k-space are recorded for different image requirements, so that sequences can be optimized. Fast acquisitions with low image quality requirements for example could only record the k-space center.

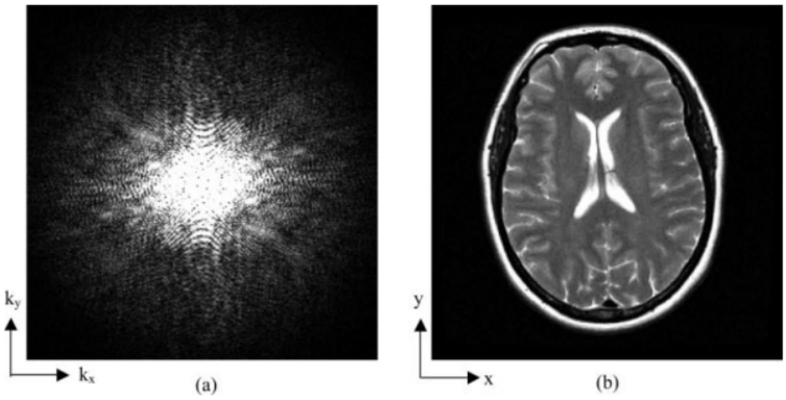

Figure 4: a) Raw k-space data of one slice in a brain measurement **b)** Image after fourier transform (reproduced from [11] with permission (CCC order license ID: 1380982-1))

TU WIEN Bibliothek Your knowledge hub
Die approbierte gedruckte Originalversion dieser Diplomarbeit ist an der TU Wien Bibliothek verfügbar
The approved original version of this thesis is available in print at TU Wien Bibliothek.

2.1.3 Hardware setup: Radio frequency coils

Evidently, a lot of hardware goes into making MRI systems work, however the component most relevant for motion detection in the scope of this thesis are the radio frequency (RF) coils. As already mentioned, they are responsible on the one hand for transmitting the transversal excitation field B_1 and on the other hand for receiving the induced magnetization changes as the MR signal. Transmit (Tx) and receive (Rx) coils can be implemented as different coils, but there is also the possibility to use transceiver (Tx/Rx) coils that act as both. The coils themselves are basically conductive loops, where the loop wires build an inductance L, with a certain resistance R and added capacitances C. This builds a resonant circuit that can create an oscillating magnetic field with the respective resonance frequency. The resonance frequency of the coil is tuned to the Larmor frequency. For receiving the reverse happens, the change in magnetic flux that happens through the transverse magnetization process induces an electric current in the coil according to Faraday's law. Relevant formulas for these processes can be looked up in [12]. One piece of hardware that is added to the receive coils and that will be important later on are the preamplifiers. Since the electric signal that is received via the magnetization is comparatively low, it is amplified directly after the coil to ensure a high signal-to-noise ratio (SNR). In figure 5, an example schematic of a basic receive coil can be seen.

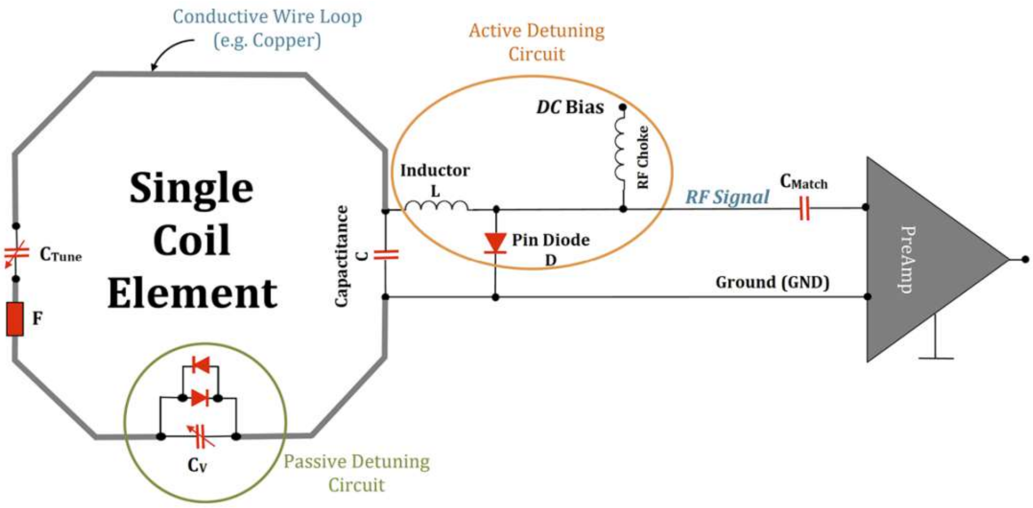

Figure 5: Schematic circuit of an RF receive coil, with capacitors for frequency tuning, a preamplifier and active and passive detuning circuits for safety during transmission (reproduced from [13] with permission (CCC order license ID: 1380983-1))

In practice not single and independent coils are used, but whole arrays of multiple coils that overlap and create a big field of view so that larger body parts can be imaged. Those arrays can be flexible or rigid and are usually tailored for specific body parts, in general for best image quality it is essential to get as close as possible to the target region. A general distinction can be made between two coil types, volume and

Die approbierte gedruckte Originalversion dieser Diplomarbeit ist an der TU Wien Bibliothek verfügbar
The approved original version of this thesis is available in print at TU Wien Bibliothek.
TU WIEN Bibliothek Your knowledge hub

surface coils. Volume coils encircle the entire body or the significant target region, e.g. the head, and are often in cylindrical shape. Surface coils are designed to fit closer to the target region and are typically flat or curved and conform to the shape of the body part being imaged. A visualization of those two types within the bore can be seen in figure 6.

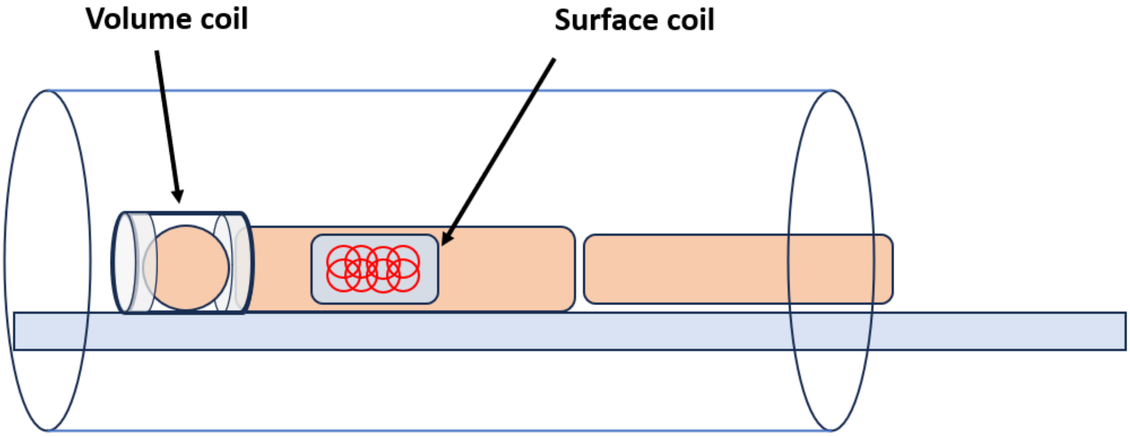

Figure 5: Visualization of volume and surface RF coil types for MRI

2.2 Patient motion in MRI

After clarifying the theoretical background of the measurement process, in the following it will be explained why patient motion is a problem, i.e. to what imaging artefacts it can lead, and possible solutions for monitoring, which is the focus of this work.

2.2.1 Motion-related imaging artefacts

The remarks in chapter 2.1 on how from local spin excitation one can arrive at a 3D image by sampling the respective k-space was always based on the assumption that the spins themselves are fixed in position. In reality, since scans can take several minutes to capture a specific volume, physiological motion and or body motion of the patient has to be expected, which perturbs the nuclear magnetization of the respective voxels. In terms of physiological motion, periodic movements like breathing and heartbeat that play a role especially in upper body measurements, and flow movements from blood or water flow in the vessels have to be considered. Additional to that random bulk movement of the body region in question by the patient due to itching for example cannot be ruled out for longer scans. Looking at the magnetization, when spins jump between voxels due to significant movement, the

Die approbierte gedruckte Originalversion dieser Diplomarbeit ist an der TU Wien Bibliothek verfügbar
The approved original version of this thesis is available in print at TU Wien Bibliothek.

amplitude is perturbed, which leads to the general problem of image blurring. The magnetization amplitudes are smoothed out over a bigger region, which has the same effect as something moving too fast in normal photography. Figure 6a) shows an example head scan with visible blurring.

The spin phases are also influenced by motion, which can lead to certain artefacts that are especially related with periodic motion. For a one-dimensional motion of spins in direction of a gradient G_x, the motion-induced phase can be calculated by $\Phi(t) = \gamma x(0) \int_0^t G_x dt' + \gamma v_x(0) \int_0^t G_x t' dt' + \frac{\gamma a_x(0)}{2} \int_0^t G_x t'^2 dt' + \ldots$ [8]. Since phase encoding is used for spatial information of the images, periodically altering the phase via movement leads to structures appearing in several parts of the image where they shouldn't be. This phenomena is called the appearance of image "ghosts". In figure 6b) an example of those ghost artefacts of a chest scan can be seen, where the chest wall is appearing multiple times in different locations due to heavy respiration. Additionally, the influence on the phase of the velocity leads to stronger dephasing and therefore a loss of signal of the affected voxels.

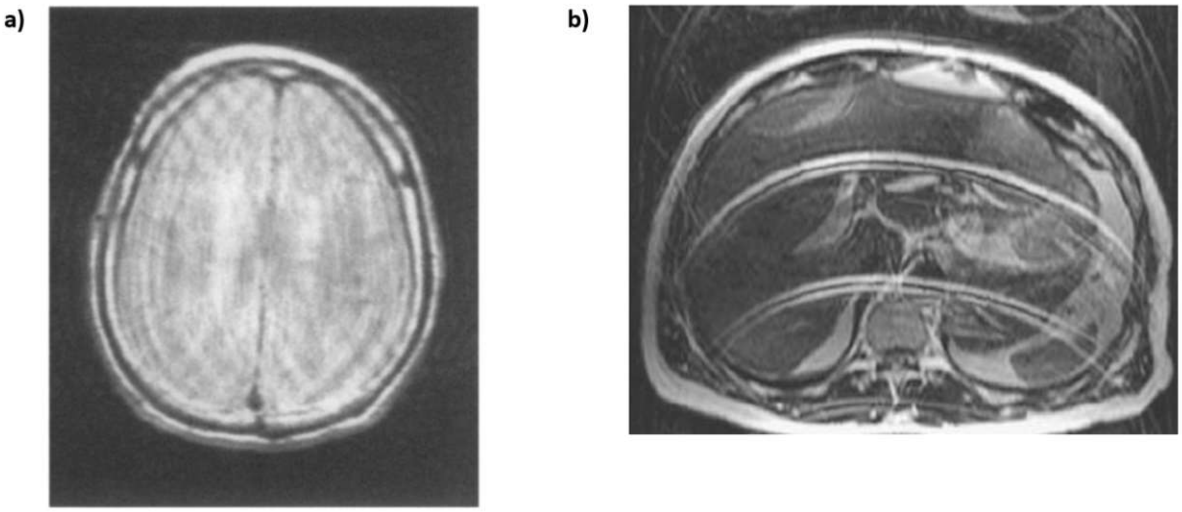

Figure 6: a) Image blurring of a head scan due to head motion (reproduced from [8] with permission (CCC order license ID: 1380984-1)) **b)** Ghost artefacts in chest scan due to periodic respiratory motion (reproduced from [14] with permission (CCC order license ID: 1380985-1))

2.2.2 Approaches in dealing with patient motion

In general, in order to deal with image artefacts due to motion, approaches can be divided into prevention and avoidance of motion right from the start, and motion tracking and correction via post-processing. To prevent bulk motion, physical restraints like cushions are used, which however are not that effective, add towards the patients discomfort and cannot prevent physiological motion. In some cases also sedation is a method of choice, which brings too much risk for the normal use case.

Die approbierte gedruckte Originalversion dieser Diplomarbeit ist an der TU Wien Bibliothek verfügbar
The approved original version of this thesis is available in print at TU Wien Bibliothek.

Independent of the patient, the imaging sequence of choice has a significant impact on the proneness towards motion artefacts. On the one hand, faster sequences can vastly diminish the influence of motion, although a compromise with the loss of general image quality has to be made, see [15]. On the other hand, using specific techniques on how the k-space is filled during a sequence can make the sequence itself more robust regarding motion artefacts independently of the time. An example for that is radial imaging, with radial k-space acquisition, see [16].

2.2.3 Motion detection methods

Since the avoidance and prevention in many cases is not sufficient, the motion has to be detected and then the images corrected regarding that motion. Tracking of patient motion can either be done by techniques regarding sequence design or external hardware. Hardware based external solutions require for example a sensor that is directly attached to the patient or something from outside of the scanner bore that is able to track the motion in one or more dimensions.

2.2.3.1 Navigators

An example with respect to sequence design are navigator echoes, first mentioned in [17]. Here a line of data in k-space is repeatedly sampled alongside the acquisition of the rest of the k-space data and this then correlates with the motion and can be used for adjusting the reconstruction.

2.2.3.2 Accelerometers and gyroscopes

As inferable from the name, accelerometers are devices that measure changes in velocity in one or more directions. The working principle is generally based on Newton’s second law of motion, stating that force is equal to mass times acceleration and usually includes masses and springs and for example a piezoelectric crystal that converts the mechanical deformation of a spring into an electrical signal. Recently, MEMS (microelectromechanical systems) solutions based in silicone technology have taken over, a good overview of possible approaches can be found in [18]. The most common technique here is a capacitive detection, where a movable mass is fixed to one movable electrode, while another corresponding electrode is anchored. Now if the mass moves the distance between the electrodes or the overlapping surface of facing electrodes changes which changes the capacitance. This can be measured and gives an electrical signal correlating with acceleration. In figure 7, two applications of that principle can be seen, one where the distance changes and one where the overlap surface changes.

TU Bibliothek WIEN Your knowledge hub
Die approbierte gedruckte Originalversion dieser Diplomarbeit ist an der TU Wien Bibliothek verfügbar
The approved original version of this thesis is available in print at TU Wien Bibliothek.

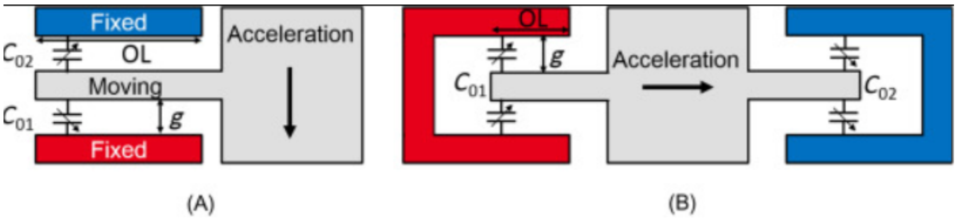

Figure 7: MEMS capacitive detection techniques **a)** Differential capacitive change where moving electrode changes gaps between fixed electrodes **b)** Surface variation between electrodes due to sliding electrode (reproduced from [18] with permission (CCC order license ID: 1381720-1))

In order to use such an accelerometer in an MRI system, it is essential that the hardware itself is non-magnetic, so it is not influenced by the magnetic field and it also doesn't influence the imaging process. Also the way the motion signal is transported outside of the scanner has to be carefully chosen so it does not affect the magnetic field. Pancoast et al. [19] proposed a wireless solution of a non-magnetic accelerometer that communicates via wifi with a Raspberry Pi outside of the scanner. This was the template for the approach in this work.

2.2.3.3 Pilot Tone

Motion detection via the so-called pilot-tone (PT) is a relatively novel and elegant method in MRI, that was first proposed in 2015 by Speier et al. [20] and subsequently established and recognized as a viable solution with many advantages [21]–[23]. This method involves the RF coils directly and uses the fact that it has been demonstrated that the load on the receive coils is altered by physiological motion [24]. Changing the coil load subsequently changes its impedance, therefore picked up signals by the coil will change in amplitude correlated with patient motion. To track this, an additional RF signal is transmitted by an external antenna that can be placed somewhere in the scanner room so that the signal reaches the receiving coils. If the antenna is at a fixed position, there are now two mechanisms modulating the picked up pilot-tone signal that are correlated with motion, one is the already mentioned change in load and secondly the path length changes geometrically with respect to the antenna and reflections and attenuation can occur due to patient motion. In figure 8 a simple pilot-tone setup with an antenna attached to the bore can be seen.

Die approbierte gedruckte Originalversion dieser Diplomarbeit ist an der TU Wien Bibliothek verfügbar
The approved original version of this thesis is available in print at TU Wien Bibliothek.
TU WIEN Bibliothek Your knowledge hub

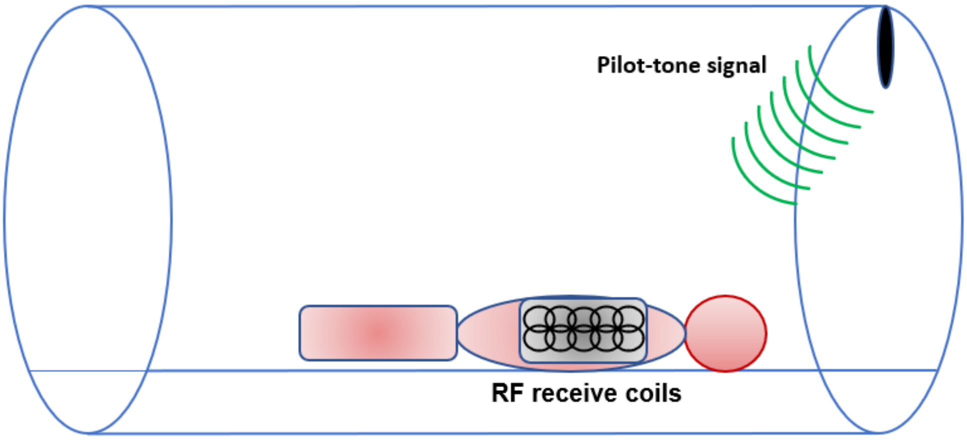

Figure 8: Sketch of a pilot-tone setup where the PT antenna is fixed to the top end of the bore

Regarding the frequency of that signal, it is essential that it on the one hand does not interfere with the imaging signal, e.g. is not too close to the Larmor frequency, but is still picked up and stored by the scanner. To deal with aliasing and wrap around artefacts, scanners by default oversample the imaging bandwidth by a factor of 2, so if the signal frequency is shifted away the right amount Δf from the Larmor frequency, it will not appear in the image but can be extracted from the raw k-space data within the oversampling bandwidth of the measurement after fourier transformation. How far the shift has to be depends on the sequence used and the specific imaging bandwidth, if it is not far enough the PT will appear as a line across the image at the specific frequency encoding position, if it is too far it won't be picked up. The advantages of the technique are that the acquisition is always synchronized with the imaging sequence and for every phase encoding step there will be a data point, so there aren't any timing issues. Also, since the sequence only determines the required frequency, it can be used for all kinds of sequences. This means it is very easy to automate and therefore perfect for clinical use. Another benefit is that since the signal is picked up by all coils of the coil array in use, it is possible to build a multi-dimensional motion model that includes the information of the specific coil location. Ludwig et al. for example built a model for respiratory compensated cardiac mri and for each coil used the formulas: [21]

$$\Delta HF_{reg} = a \cdot PT + b \tag{11}$$

$$\Delta AP_{reg} = m \cdot PT + n \tag{12}$$

where HF is the motion in head-feet direction and AP in anterior-posterior direction, PT is the amplitude of the pilot-tone signal and a,b,m and n are the model parameters.

Die approbierte gedruckte Originalversion dieser Diplomarbeit ist an der TU Wien Bibliothek verfügbar
The approved original version of this thesis is available in print at TU Wien Bibliothek.

A good overview over the process of extracting the PT signal from the raw data can be seen in figure 9, taken from [23]. In a) the mentioned frequency shift from the Larmor frequency is visible, which in this case is ~100 kHz, while in b) the corresponding raw data is visualized, where for every phase-encoding step the measured frequency spectrum is plotted, including all the image data and the pilot tone on the edge. The amplitude modulation of the pilot-tone is then analyzed in time and the resulting breathing curve after some post-processing can be seen in c).

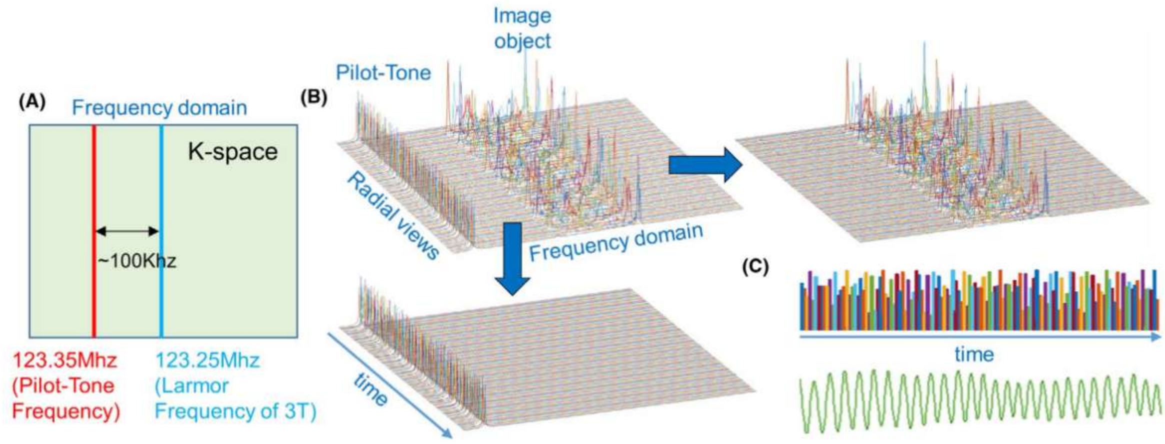

Figure 9: Pilot tone processing sequence **a)** Frequency shifting of pilot-tone signal **b)** Raw data of corresponding measurement **c)** Resulting pilot-tone amplitude modulation corresponding to breathing curve (reproduced from [23] with permission (CCC order license ID: 1381721-1))

One problem of the pilot-tone setup as described is, that since the Larmor frequency is around 123 MHz for 3T, the required pilot-tone signal has a wavelength of a few meters, making it relatively insensitive towards small movements like heartbeat or shallow breathing.

2.2.3.4 Beat Pilot Tone

A solution for that problem was proposed by Anand and Lustig in 2021, namely the Beat pilot-tone (BPT) [25]. This approach uses the fact that the preamplifiers used for the RF coils don't behave perfectly linear, allowing second order intermodulation. If two waves with frequencies f_1 and f_2 are mixed by a nonlinear electronic component, the resulting so called heterodyne signal contains components of a signal with the differential frequency $f_1 - f_2$ and also one with the summed frequency $f_1 + f_2$. Following [26], [27], when expanding the nonlinear function F into a power series:

$$F(v) = \alpha_1 v + \alpha_2 v^2 + \alpha_3 v^3 + \ldots \tag{12}$$

and adding the two sine waves with a frequency of $\omega_1 = 2\pi f_1$ and $\omega_2 = 2\pi f_2$ as an input, the resulting frequency:

Die approbierte gedruckte Originalversion dieser Diplomarbeit ist an der TU Wien Bibliothek verfügbar
The approved original version of this thesis is available in print at TU Wien Bibliothek.

$$v_{out} = F(A_1 cos(\omega_1 t) + A_2 cos(\omega_2 t)) \tag{13}$$

including the first two orders can be calculated according to:

$$v_{out} = \alpha_1 (A_1 cos(\omega_1 t) + A_2 cos(\omega_2 t)) + \alpha_2 (A_1 cos(\omega_1 t) + A_2 cos(\omega_2 t))^2 + ... \tag{14}$$

With some simplification using trigonometric identities, the two heterodyne terms can be identified in the result among many other terms:

$$v_{out} = ... + \alpha_2 A_1 A_2 cos(\omega_1 - \omega_2)t + \alpha_2 A_1 A_2 cos(\omega_1 + \omega_2)t \tag{15}$$

For the beat pilot-tone application this means that if two higher frequencies have the correct differential frequency, the two higher frequency signals can be used for more precise motion sensitivity, while simultaneously the result is still captured within the scanner bandwidth after passing the preamplifier. For this if the frequency of one signal is f_1, the frequency of the second signal has to set to $f_2 = f_1 + f_{Larmor} + \Delta f$, where Δf shifts the BPT signal into the oversampling bandwidth as described above. If for example two signals with a frequency within the small GHz range are used, the wavelength diminishes to a few centimeters compared to meters with the pilot tone technique. Figure 10 shows a sketch of a setup where an antenna behind the bore sends the two desired frequencies that are picked up by the coil, and figure 11 visualizes the concept of the two frequencies being separated by the desired pilot-tone frequency which is then processed by the preamplifier.

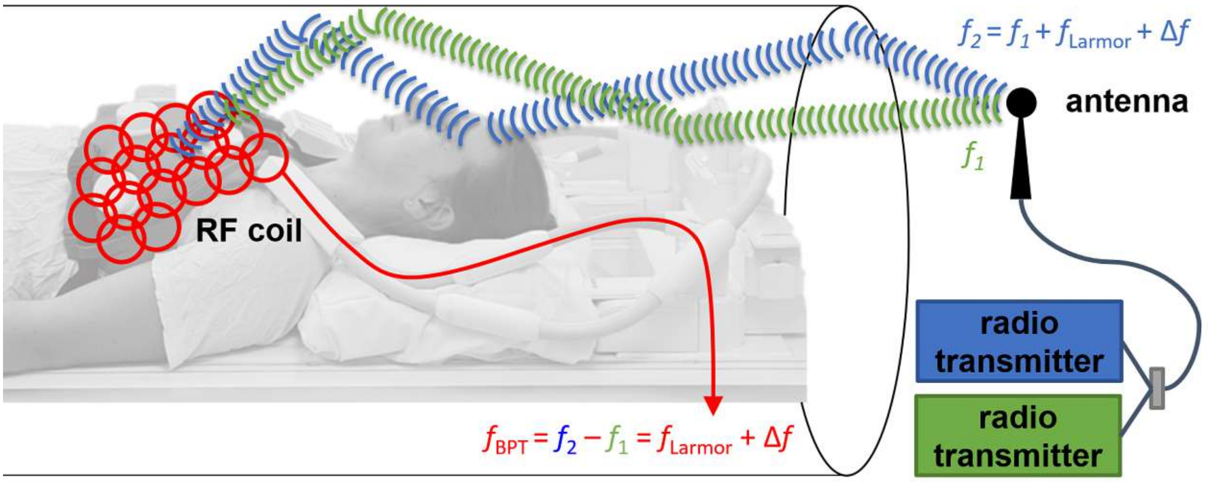

Figure 10: Sketch of a beat pilot-tone setup where the BPT antenna is placed behind the bore

Die approbierte gedruckte Originalversion dieser Diplomarbeit ist an der TU Wien Bibliothek verfügbar
The approved original version of this thesis is available in print at TU Wien Bibliothek.

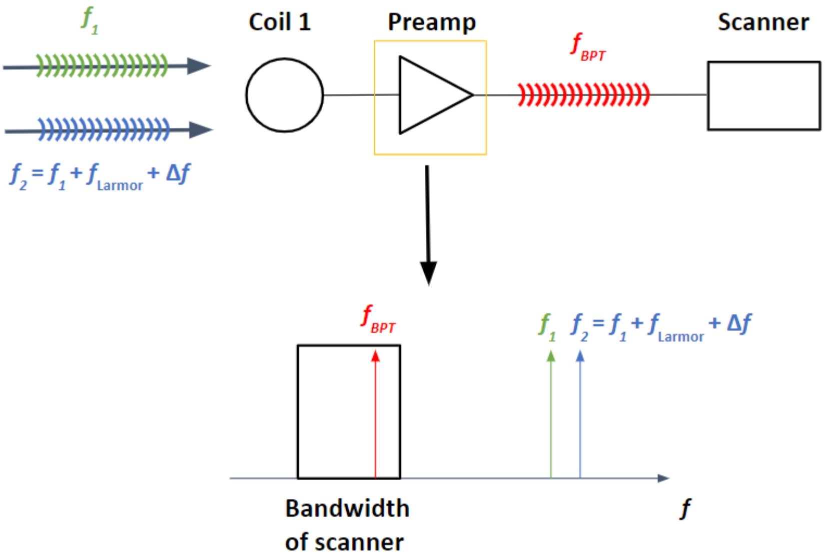

Figure 11: Beat pilot-tone processing with the intermodulation at the preamplifier

Lamar-Bruno et al. were able to demonstrate in 2022 that using the BPT provides a significantly improved motion sensitivity over using a single PT and a remarkable improvement in image quality could be achieved [28].

2.2.3.5 Other hardware-based methods

Another method based on external hardware is to extract the motion directly from a video using optical sensors like cameras, see [29] or [30]. Here a MR compatible camera is attached for example to the top of a head coil. The movement of the head can then be calculated by tracking of optical markers attached to the face of the patient, or directly by automatic recognition of facial features. A hardware sensor that similarly to the accelerometers can be directly attached to the patient is a magnetic field motion tracking sensor, see for example [31]. Here the sensor is made up of three orthogonal pairs of pickup coils measuring the current magnetic field and its location can be afterwards calculated by using the information of the native gradient fields of the scanner.

2.2.4 Motion correction methods

After acquiring the motion information via the aforementioned various methods, they have to be implemented in some way to correct the resulting images. This task can be distinguished in prospective and retrospective motion correction. In prospective motion correction, e.g. [32], the motion information is used for real-time adjustment of the imaging pulse sequence. For example when a rotation happens, the directions of the gradients are modified so that every voxel experiences the same field it would without the rotation. After that a normal reconstruction should lead to improved

Die approbierte gedruckte Originalversion dieser Diplomarbeit ist an der TU Wien Bibliothek verfügbar
The approved original version of this thesis is available in print at TU Wien Bibliothek.

images with less motion artefacts. Retrospective motion correction however is applied after the scan is finished, and the motion information is combined with specific algorithms to adjust the image reconstruction for motion. One correction algorithm, which is also the one used for correction in this thesis, is the so-called Generalized Reconstruction by Inversion of Coupled Systems (GRICS) algorithm, which was first proposed by Odille et al. in 2008 [33]. Here the reconstruction is approached as two inverse problems. One is the construction of a motion model, consisting of a spatial transformation operator created by the measured motion, and the other one is a motion model optimization, where the reconstruction residue is minimized. With this algorithm multi-dimensional correction is possible using the information e.g of multiple coils after a beat pilot-tone acquisition.

Die approbierte gedruckte Originalversion dieser Diplomarbeit ist an der TU Wien Bibliothek verfügbar
The approved original version of this thesis is available in print at TU Wien Bibliothek.

3 Materials and Methods

In this chapter the hardware and software that was used for constructing the motion monitoring setups within this thesis will be specified, as well as the tools that were utilized for test measurements. First, a setup with a wireless accelerometer-based motion sensor is described and then secondly, a setup employing the beat pilot tone.

3.1 MRI compatible wireless motion sensor

As previously mentioned, the wireless motion sensor setup mainly followed the setup that was made openly accessible by Pancoast et al. [19]. Some of the hardware pieces were different leading to adjustments that had to be made to the software.

3.1.1 Hardware

Sensor

The sensor used was the LIS331HH (STMicroelectronics, Plan-les-Ouates, Switzerland), a MEMS based low-power high performance three axes linear accelerometer. It is based on capacitive detection technology and is sensitive up to an accuracy of 0.003 *g* of acceleration in the respective three dimensions with a maximum output data rate of 1 kHz. [34] Its data can be accessed via a digital I^{2}C or a SPI serial interface standard output. In figure 12 a picture of the used sensor and the block diagram can be seen.

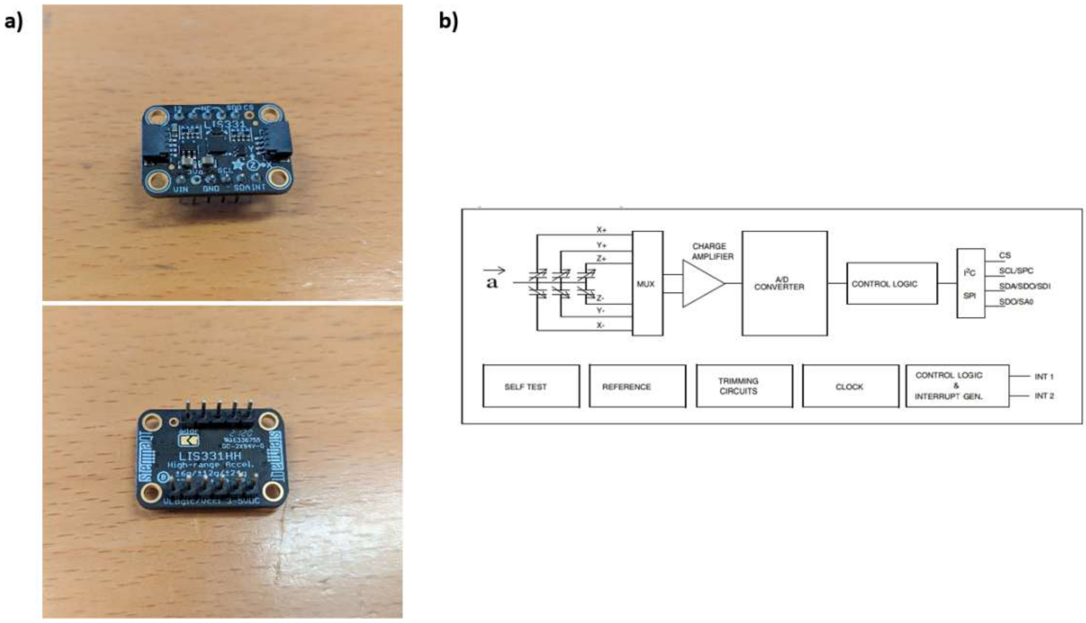

Figure 12: LIS331HH accelerometer **a)** Used sensor for the experiments **b)** Block diagram of the sensor [34]

Die approbierte gedruckte Originalversion dieser Diplomarbeit ist an der TU Wien Bibliothek verfügbar
The approved original version of this thesis is available in print at TU Wien Bibliothek.
TU WIEN Bibliothek Your knowledge hub

Die approbierte gedruckte Originalversion dieser Diplomarbeit ist an der TU Wien Bibliothek verfügbar
The approved original version of this thesis is available in print at TU Wien Bibliothek.

Microcontroller setup

As a microcontroller to process the data from the sensor a feather board (ESP32-WROOM-32U, Adafruit, New York, USA) was used, which was connected to the sensor via I^2C over a PCB. A wifi antenna (W3921, Pulse Electronics, San Diego, USA) was soldered to the chip for data transmission. This whole setup was powered by a 3V lithium polymer battery connected to the feather board. A lithium polymer battery was chosen due to its non-magnetic behavior. In figure 13 the finished setup that is able to send a wireless motion signal can be seen from three angles.

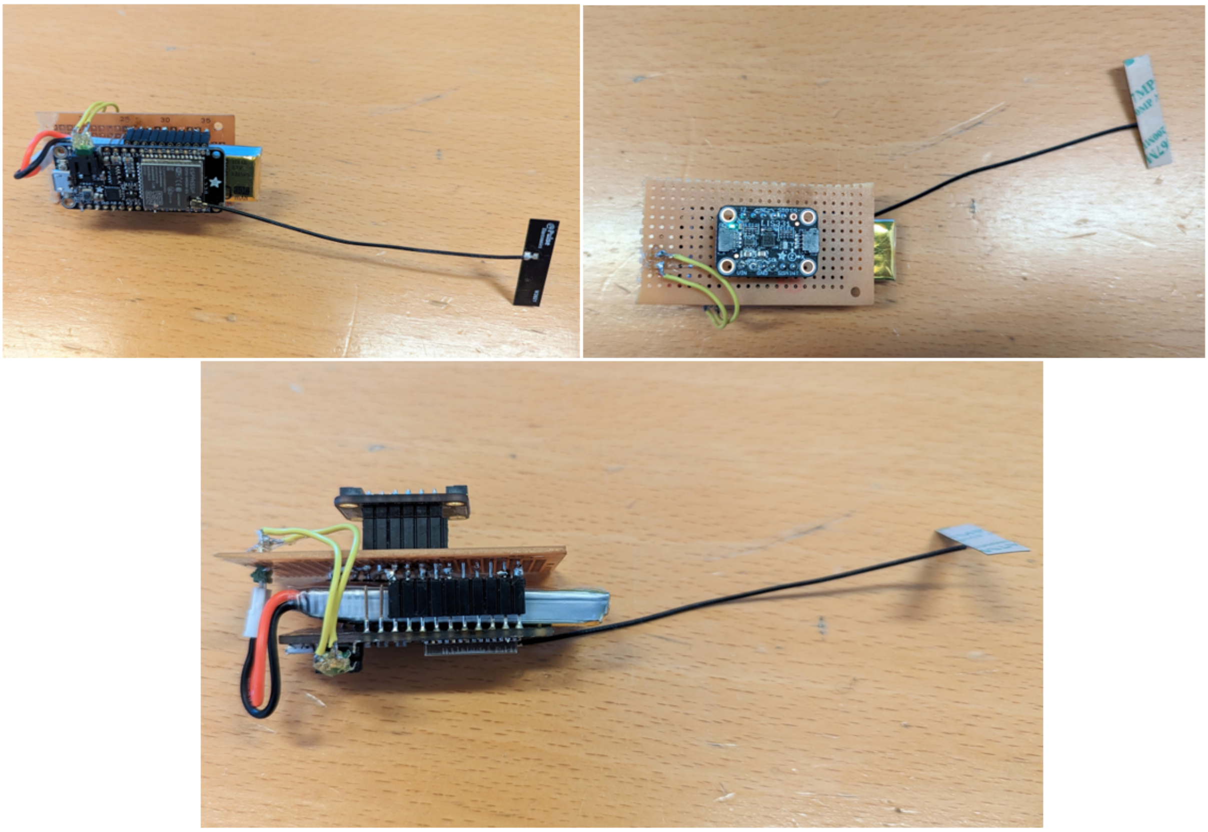

Figure 13: Wireless sensor setup including the LIS33HH, an ESP32 feather board with an attached WIFI antenna and a 3V lithium polymer battery

Faraday cage

In order to ensure some shielding of the sensor electronics from electromagnetic fields in the MR scanner, a simple Faraday cage was built for first tests. A Faraday cage is based on Faraday’s law of electromagnetic induction, which implies that if a space is entirely enclosed by an electric conductor that an external electromagnetic field can’t penetrate into the space inside, due to the resulting charge distribution in the conductor. [35] This is for example also used for the MR scanner room itself, which is basically a huge Faraday cage that shields the setup from RF interference from outside. For this application a small box with a sliding lid was 3D printed, using polylactic acid (PLA) as a filament. Copper foil was then pasted to the surface inside to create a closable space with a continuous surface of conducting copper foil for the sensor setup. The result can be seen in figure 14.

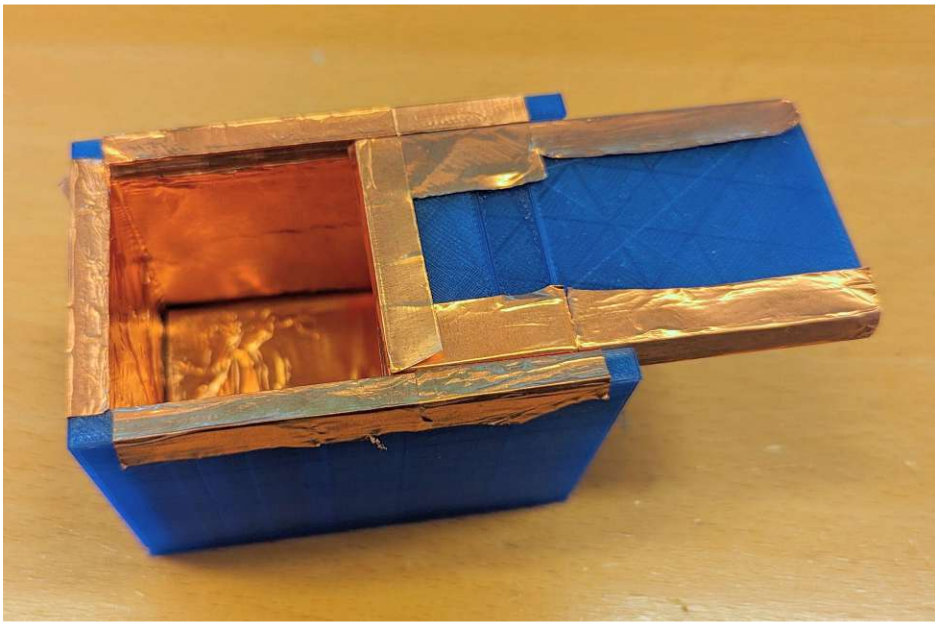

Figure 14: 3D printed PLA Faraday cage with copper foil for conducting enclosure

Processing unit

In order to control the sensor and receive the data a Banana Pi was used, which is a single-board computer similar to the well known Raspberry Pi. Ubuntu was installed as the operating system and an USB WIFI stick plugged in for the connection.

3.1.2 Software

For the communication between the Banana Pi and the ESP32 some supplementary software had to be installed, enabling WIFI access. RaspAP was used as a tool on the Banana Pi so that it could act as a WIFI router and therefore an access point for the microcontroller. Mosquitto in combination with NodeRED were the tools used enabling and organizing the communication between the devices, providing an interface displaying the current measurement and sensor information and making it possible to save measurement data directly to the Banana Pi. The NodeRED flow used was identical to the one provided by Pancoast et al.. For the microcontroller, Visual Studio Code with PlatformIO was used to compile and upload the necessary code that governs the sensor side of the communication. This again was similar to the provided script, however some things regarding the sensor had to be changed

Die approbierte gedruckte Originalversion dieser Diplomarbeit ist an der TU Wien Bibliothek verfügbar
The approved original version of this thesis is available in print at TU Wien Bibliothek.
TU WIEN Bibliothek Your knowledge hub

since a LIS331HH was used instead of the BNO08x, the code can be found in the appendix. Figure 15 shows the interface output that can be accessed on the Banana Pi via an internet browser, showing a plot of the current acceleration measurement with meta data and save options.

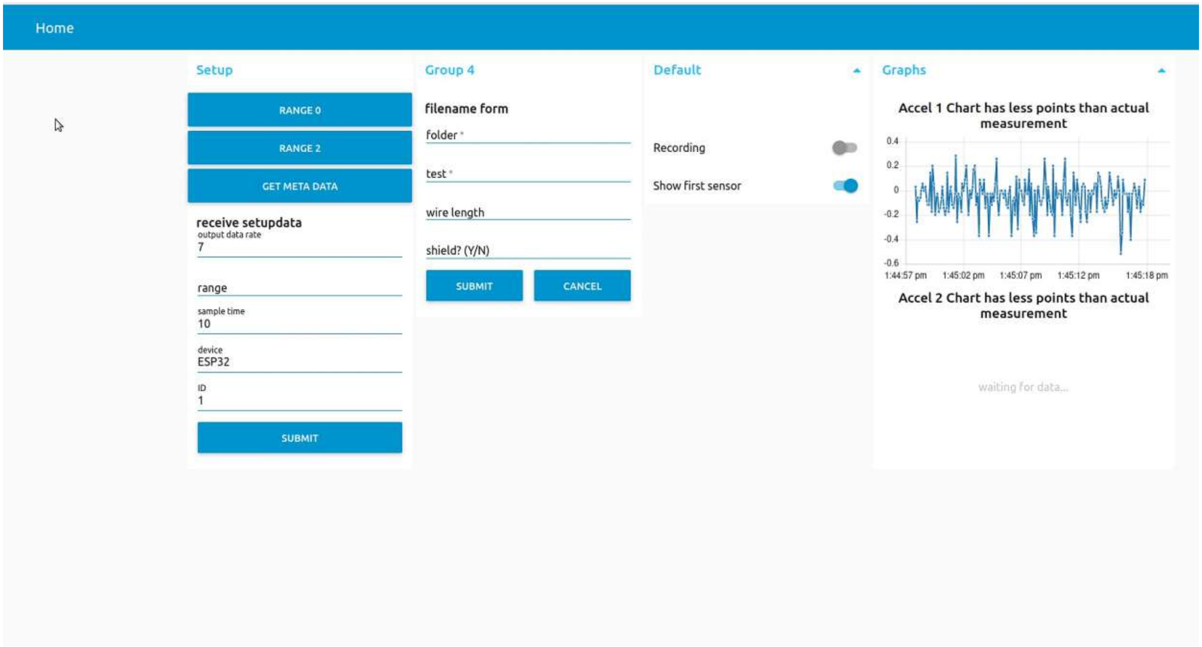

receive setupdata

output data rate: 7

range:

sample time: 10

device: ESP32

ID: 1

filename form

folder *:

test *:

wire length:

shield? (Y/N):

Recording: ○

Show first sensor: ●

Figure 15: NodeRED interface to interact with the sensor on the Banana Pi including save options

3.1.3 Measurements

For measurements in the MR scanner, the Banana Pi was led through a waveguide next to the entrance into the scanner room to ensure that the signal can be picked up via wifi. The rest of the computer hardware was placed outside so that it is not affected by the magnetic field and everything could be controlled during the scan process. In figure 16 a sketch of the setup in the scanner room can be seen, where the scanner inside of the faraday cage is placed on a spherical MR phantom inside of the bore, sending the movement signals to the Banana Pi next to the entrance door. This was the first test setup used in order to check the different hardware parts for their magnetic properties and artefact behavior.

Die approbierte gedruckte Originalversion dieser Diplomarbeit ist an der TU Wien Bibliothek verfügbar
The approved original version of this thesis is available in print at TU Wien Bibliothek.
TU WIEN Bibliothek Your knowledge hub

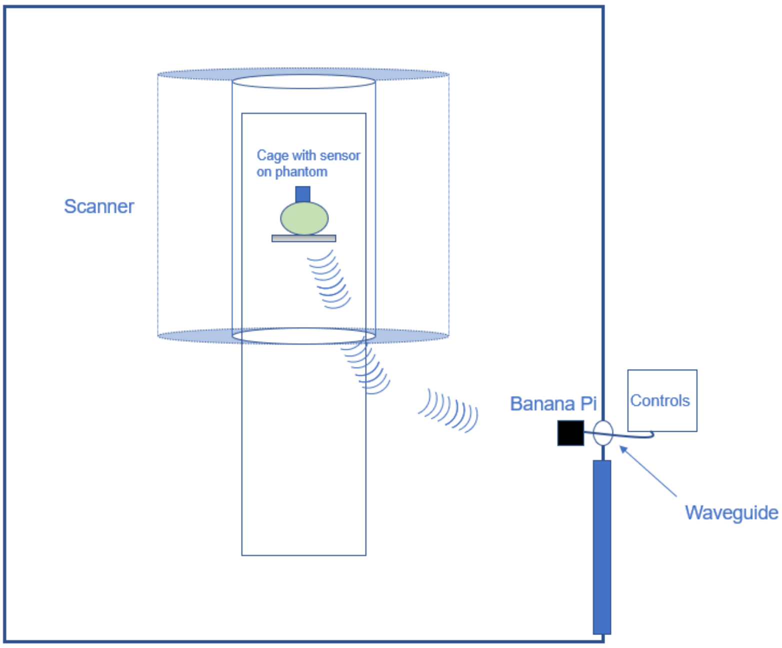

Figure 16: Test setup in scanner with sensor in faraday cage on spherical phantom and Banana Pi connected through waveguide next to the scanner room door

The spherical phantom with the faraday cage attached to the top via duct tape can be seen in figure 17. A basic gradient echo sequence (TR = 300 ms, TE = 15 ms) at a 3T Siemens MAGNETOM Prisma scanner was used to capture some test images with different contents of the cage. The contents were varied according to:

1. Reference without cage
2. Cage only
3. Cage with battery
4. Cage with running sensor setup with antenna kept inside
5. Cage with running sensor setup with antenna reaching outside
6. Cage with sensor and battery without PCB

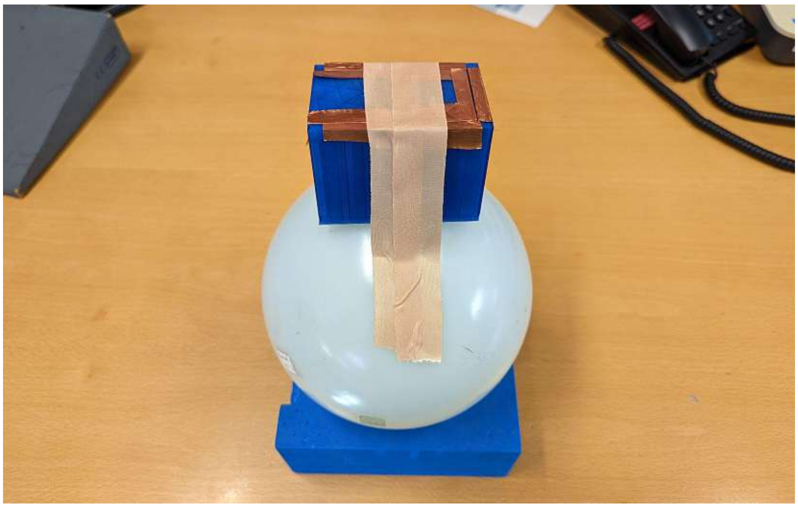

Figure 17: Spherical phantom setup with faraday cage and sensor setup attached to the top

Die approbierte gedruckte Originalversion dieser Diplomarbeit ist an der TU Wien Bibliothek verfügbar
The approved original version of this thesis is available in print at TU Wien Bibliothek.

3.2 Beat Pilot Tone

The procedure to test and build a functioning BPT setup was split into two steps, at first to examine the general functionality and principle, a test setup in the laboratory was built, followed by the actual setup used for measurements in the MR scanner.

3.2.1 Setup in laboratory

3.2.1.1 Hardware

Signal generators

To generate the two RF waves necessary for creating the BPT signal two different signal generators were used, due to availability. Requirement was that they could deliver a stable and precise signal within the GHz range, that is manually tunable. One was a Rohde&Schwarz SM300, that can generate RF signals from 9 kHz to 3 GHz with a power level of up to 13 dBm. The second one was a Crystek CRBV55BE-1000-2000, which is a voltage-controlled oscillator that can generate RF signals from 1 GHz to 2 GHz with a power level of up to 9 dBm.

Transmitting antenna and receive coil

For transmission of the signal, the two RF signals were combined by a tee connector and then led to a pre-built single coil that acted as the antenna for both signals. The receive coil used for picking up the signals was a pre-built 3T coil element, including an active detuning circuit and a preamplifier (MPB-123R20-90, HiQA, Ottawa, Canada)), where the BPT signal emerges. Figure 18 shows both coil pieces.

Die approbierte gedruckte Originalversion dieser Diplomarbeit ist an der TU Wien Bibliothek verfügbar
The approved original version of this thesis is available in print at TU Wien Bibliothek.
TU WIEN Bibliothek Your knowledge hub

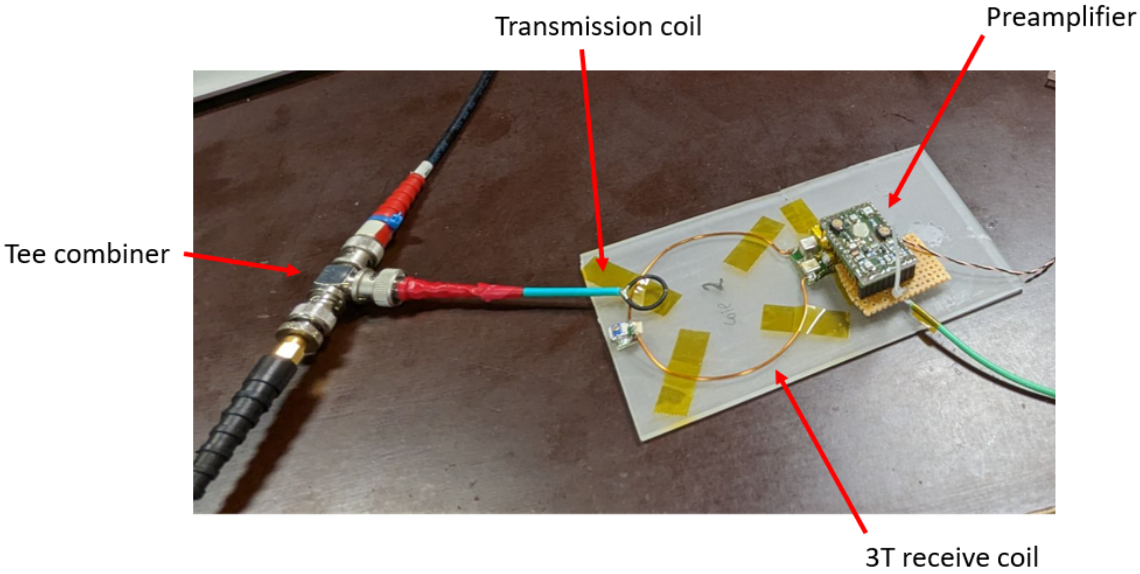

Figure 18: Transmission and receive coils for laboratory test setup

Network analyzer and test rig

The receive coil is connected to an MR test rig, emulating the behavior of a Siemens MR scanner using Siemens TIM connectors. This test rig is connected to an E5071C vector network analyzer (VNA) by Agilent Technologies, that can analyze signals from 100 kHz to 6.5 GHz and measures s-parameters (scattering parameters) of electrical networks. The VNA was set to display the amplitudes of the received RF signals around the Larmor frequency of 123 MHz for the BPT signal and around the transmission frequencies of 1 and 1.123 GHz. The simultaneous and live display of those frequency spectra was used to calibrate the setup and find the right transmission power in order to ensure a BPT signal with a sufficient amplitude.

3.2.1.2 Software

To record and analyze the frequency data captured by the VNA, it provides an option to save the current trace data to a CSV file. Since this is only a momentary capture and continuous data is needed for the motion analysis, a key macro was scripted using AutoHotkey that enabled several data saves per second by continuous pressing of a specified key. Since the maximum refresh rate of the VNA is 205 ms, around 5 data points per second could be retrieved enabling an analysis regarding breathing motion.

Matlab R2021a was used for the data analysis, implementing a simple peakfinder routine to track the amplitude of the BPT signal peak.

Die approbierte gedruckte Originalversion dieser Diplomarbeit ist an der TU Wien Bibliothek verfügbar
The approved original version of this thesis is available in print at TU Wien Bibliothek.
TU Bibliothek WIEN Your knowledge hub

3.2.1.2 Measurements

Once the BPT signal was successfully visible on the VNA, ensuring that the setup properly works, a measurement including a breathing subject was taken, testing the capability of the BPT to capture motion. For this the coil element was taped to the chest of the subject lying on the bench, with the transmission antenna fixed to a tripod closely above. Figure 19 shows the complete setup with the subject with the coil on his chest and the VNA in the back that shows the different signals on the monitor as described above. For the measurement the subject was told to take three deep breaths, while the experimenter recorded exactly for that time. For the BPT signal this should result in three periodic up and down movements of the amplitude, if the motion sensitivity is given.

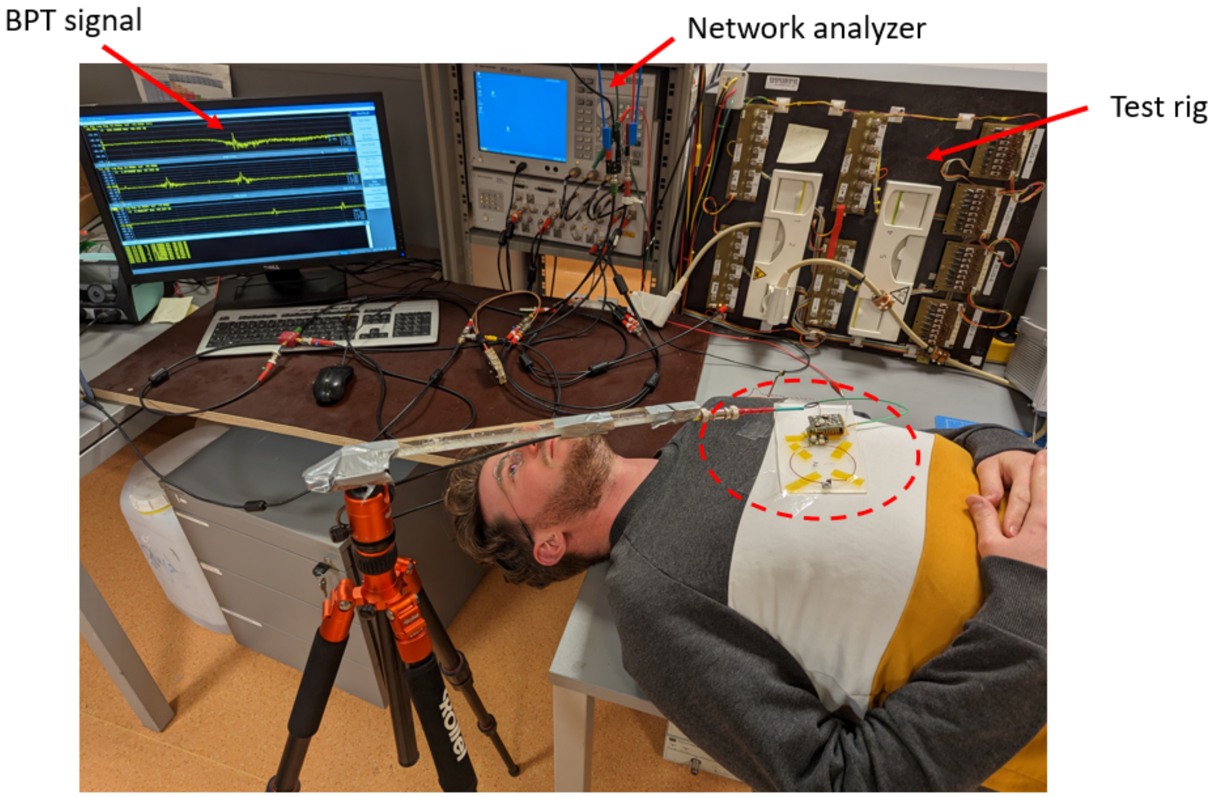

Figure 19: Complete test setup including a heavy breathing subject to test motion sensitivity of BPT signal

Die approbierte gedruckte Originalversion dieser Diplomarbeit ist an der TU Wien Bibliothek verfügbar
The approved original version of this thesis is available in print at TU Wien Bibliothek.

Die approbierte gedruckte Originalversion dieser Diplomarbeit ist an der TU Wien Bibliothek verfügbar
The approved original version of this thesis is available in print at TU Wien Bibliothek.

3.2.2 Setup in scanner

3.2.2.1 Hardware

Signal generators and antenna

The RF boards used to create the necessary signals were the USRP B210 SDR dual channel transceivers by Ettus Research, as used by Anand and Lustig [25]. They have a continuous RF coverage of 70 MHz - 6 GHz, with an architecture based on a field-programmable gate array (FPGA), allowing software defined radio (SDR) outputs accessible via USB 3.0. Their power output can reach up to 10 dBm and they have a frequency accuracy of ±2 ppm. Two boards were used to separately create the two signals with the required BPT difference frequency, then combined with a tee connector and led to a WIFI antenna (ANT-5GWWS6-SMA, TE Connectivity, USA) via a 10 m coaxial cable. In figure 20 both pieces of hardware can be seen.

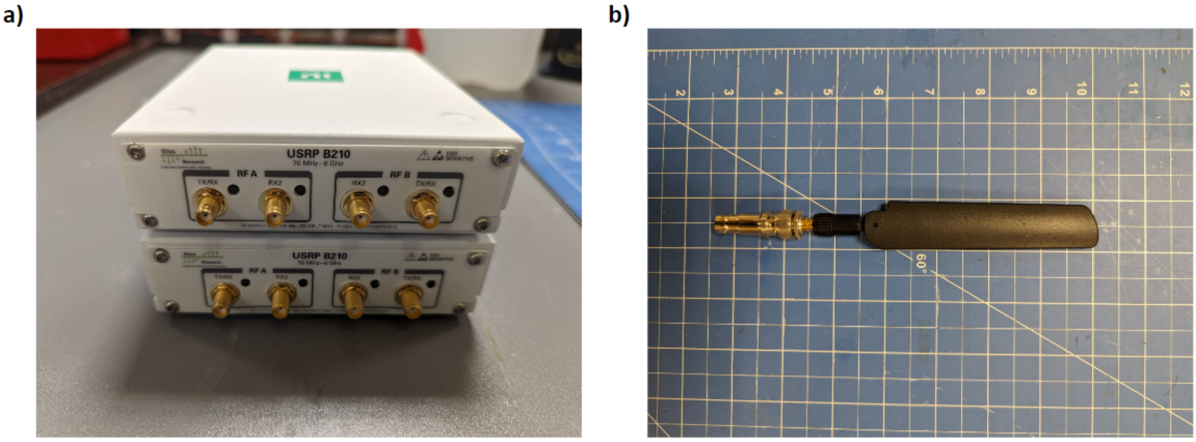

Figure 20: **a)** Ettus Research USRP B210 SDR dual channel transceivers **b)** ANT-5GWWS6-SMA WIFI antenna

Coil Arrays

In order to test the behavior of the setup with different coil arrays, three different arrays were used for the BPT test measurements. The first one was “ModFlex”, which is a modular system of flexible lightweight 4-channel coaxial receive-only coil arrays, developed at the same research group by Nohava et al. [36]. Due to its versatility and robust coil characteristics, this coil array can be used for many different body parts, including chest measurements for this setup, providing a very flexible and individual fit for the subject. The comparatively low amount of channels also and concise target region with one module allows for fast data processing. Figure 21 shows how a ModFlex with two 4-channel modules is assembled.

Die approbierte gedruckte Originalversion dieser Diplomarbeit ist an der TU Wien Bibliothek verfügbar
The approved original version of this thesis is available in print at TU Wien Bibliothek.
TU WIEN Bibliothek Your knowledge hub

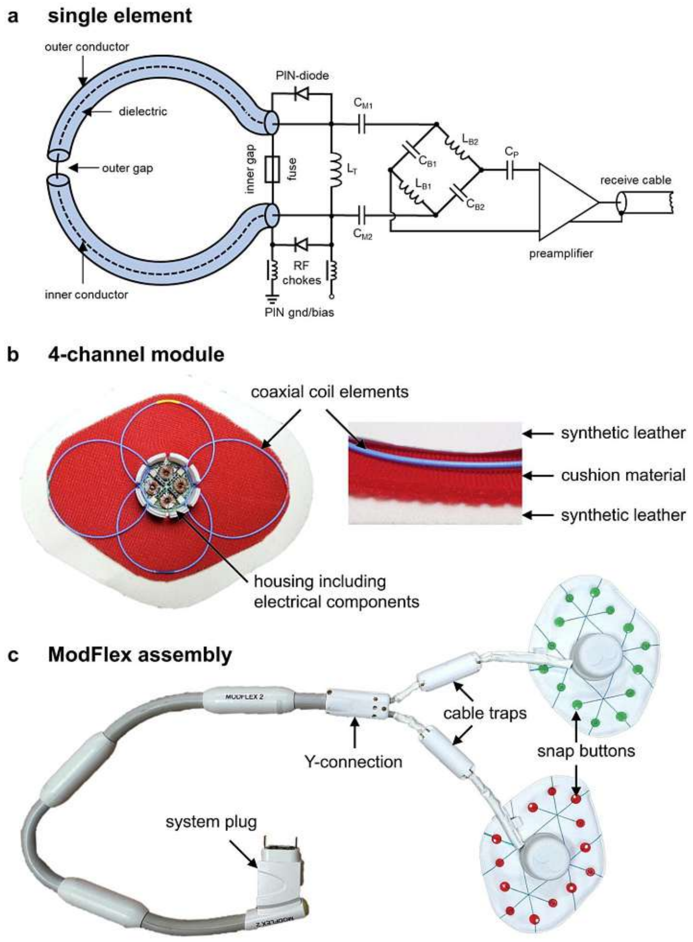

Figure 21: ModFlex coil design **a)** Circuit of one coaxial coil element **b)** 4-channel module assembly **c)** Two 4-channels modules within housing including connector to MR system (reproduced from [36] with public permission)

The second coil array used was a flexible coil array specifically tailored for breast imaging, the so-called “BraCoil”, developed by Obermann and Nohava et al. [3]. This wearable coil vest was manufactured to enable precise and comfortable breast cancer screening, by chest MRI acquisition in supine position with high image quality. It is assembled incorporating 28 coaxial receive-only coil elements, with 4-channel modules similar to those in the “ModFlex”. The vest is constituted of several textile layers, making it flexible and includes waist and shoulder belts to adjust and closely fit the coil array to the subject’s breast. The supine position potentially leads to motion due to breathing, making it a prime target for motion correction using the beat pilot-tone. In figure 22 the layout and coil design of the ”BraCoil” can be seen.

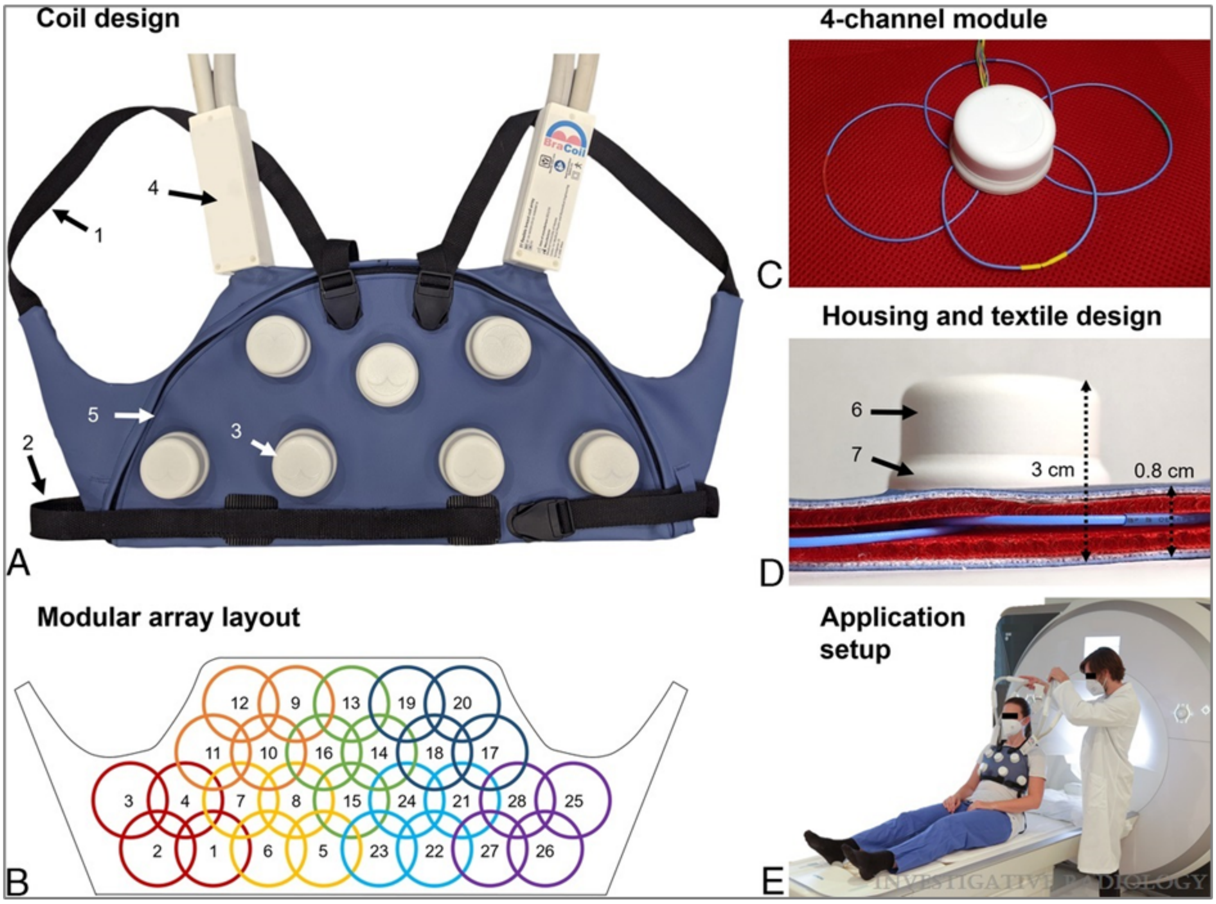

Figure 22: “BraCoil” assembly and design **a)** Outward appearance of flexible vest **b)** Array layout of the 28 coil channels **c)** Example 4-channel module **d)** Cross-section of housing and textile **e)** Example of application with patient (reproduced from [3] with public permission)

The third coil array used was the so-called “Body 18” coil (Siemens Healthineers, Erlangen, Germany), which is an 18-channel lightweight coil array with a rectangular semi-flexible housing, that can be clipped onto the patient table and fixated on top of the thorax of the subject, allowing for chest measurements. It consists of 3 rows of 6 elements each and the coil set-up for chest measurements can be seen in figure 23. The coil array was chosen as a third and external option, ensuring that the BPT setup also works similarly with commercial and established coil arrays.

Die approbierte gedruckte Originalversion dieser Diplomarbeit ist an der TU Wien Bibliothek verfügbar
The approved original version of this thesis is available in print at TU Wien Bibliothek.
TU WIEN Bibliothek Your knowledge hub

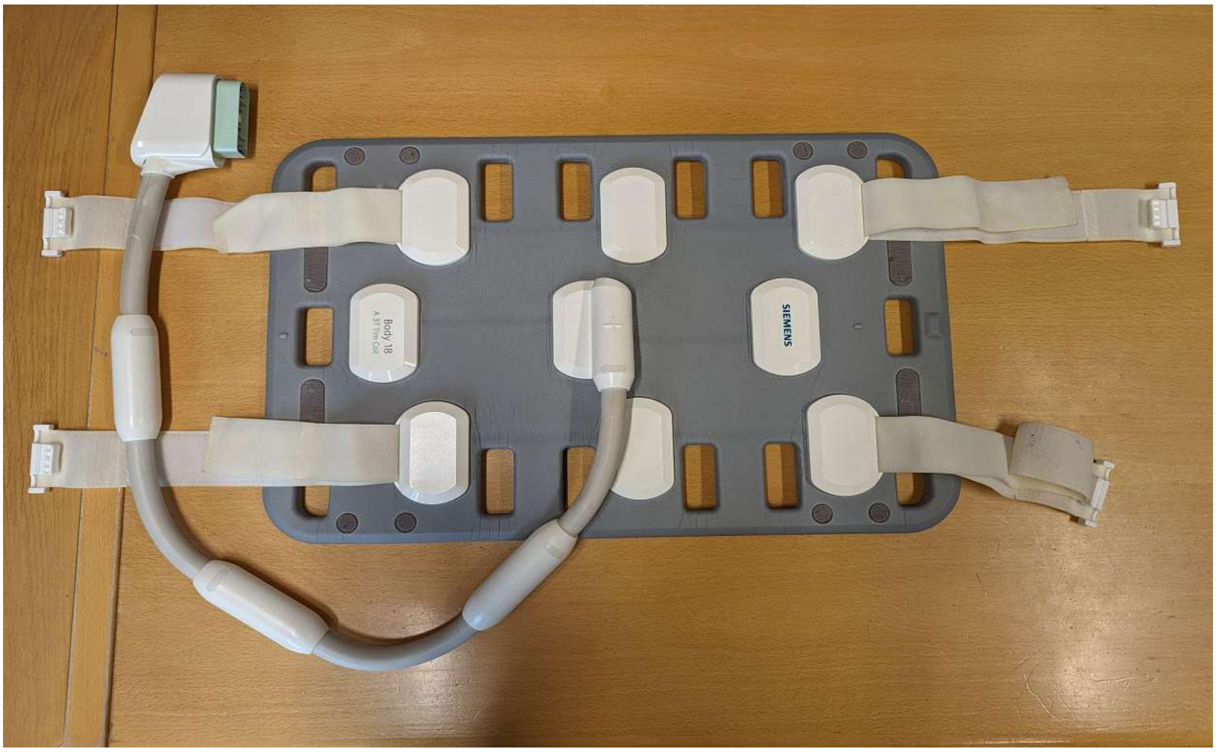

Figure 23: Body 18 coil by Siemens used for chest measurements

Scanner

The scanner that was used to conduct the measurements was a 3T Siemens MAGNETOM Prisma.

3.2.2.2 Software and post-processing

Signal control

The B210 transceiver boards were controlled by an example script provided after installation of the necessary software to communicate with the board over USB. The script can be started via the command prompt and makes the board transmit an RF signal at the specified antenna port, with custom frequency and power gain.

Data analysis

To analyze the raw data that is generated by the scanner Matlab R2021a and mapVBVD.m [37] was used, which is a tool to read MRI raw data produced by Siemens scanners. This was used to get the whole k-space matrix of the measurement in acquisition order, which is then squeezed and summed along the dimension of the turbo factor, to result in a data matrix with the dimensions *frequency*

Die approbierte gedruckte Originalversion dieser Diplomarbeit ist an der TU Wien Bibliothek verfügbar
The approved original version of this thesis is available in print at TU Wien Bibliothek.

encoding x channel x phase encoding x slice. An inverse Fourier transform is applied to obtain the respective amplitudes of the imaging data, which contains the recorded BPT peak in the oversampling area. Figure 24 shows an example plot where for one specific slice the frequency spectrum of each phase encoding step is plotted and superimposed. In the center around the Larmor frequency the actual MR signal within the imaging bandwidth can be seen, while on the right in the oversampling bandwidth the BPT peak is located exactly with the adjusted offset to the center.

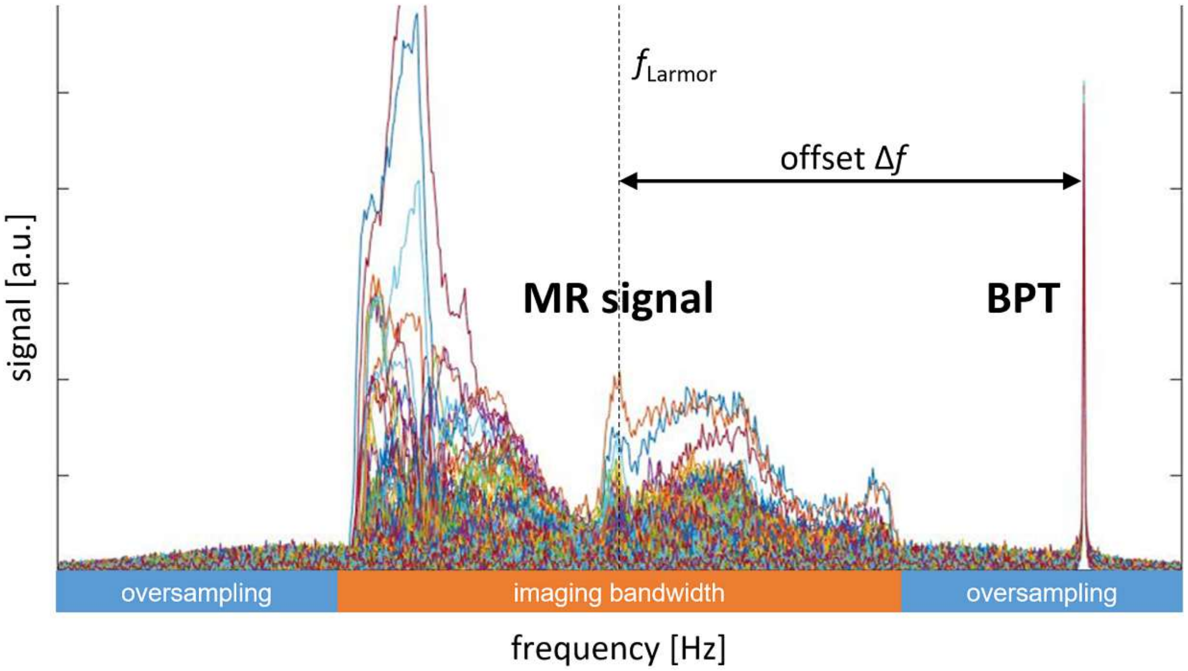

Figure 24: Example raw data with BPT signal and MR signal, the beat pilot tone signal is seen on the right side, with the desired offset from the Larmor frequency.

To analyze the evolution of the BPT amplitude with time, the peak data is integrated along its width for every channel. The respective timestamps can be taken from the k-space struct created in the beginning by the mapVBVD function. In order to filter the resulting time-courses of the BPT amplitude and remove the noise, a low pass filter with a cutoff of 0.5 Hz was applied. After filtering the time-courses are normalized to a range from -1 to 1. The relevant Matlab code can be found in the appendix.

Image reconstruction and correction

Reconstructing the images using the extracted BPT time-courses for motion correction was done by Karyna Isaieva from the Diagnosis and Interventional Adaptive Imaging (IADI) unit of the University of Lorraine, France. The reconstruction is based on the Generalized Reconstruction by Inversion of Coupled Systems (GRICS) algorithm, which was first proposed by Odille et al. in 2008 [33].

Die approbierte gedruckte Originalversion dieser Diplomarbeit ist an der TU Wien Bibliothek verfügbar
The approved original version of this thesis is available in print at TU Wien Bibliothek.

3.2.2.3 Measurements

Setup

To get the transmission antenna as close as possible to the RF coil, three different setups were used that are all shown in figure 25. Setup a) used a BNC port that is located on the backside of the scanner room and grants access via a penetration panel. One coaxial cable led from the B210 radio transmitters towards the port on the outside, while another one led from the inside port towards the antenna, which in this case was fixed to the top of the bore with duct tape. Setup b) used the waveguide next to the entrance door, to direct one coaxial cable directly from the transmitters outside to the antenna inside, which was fixed to a tripod behind the bore. The variations in antenna position and cable laying was done to test for potential interferences due to motion of the antenna triggered by the gradients or due to signals transported inside of the scanner bore via the cables. Finally in the third setup, the antenna was fixed directly inside of the bore above the patient. Additionally, floating cable traps were put on the coaxial cable to block induced shield currents and a 10 MHz sync signal from the scanner was applied to the radio transmitters to synchronize the two signals. Figure 26 shows setup a) with the antenna attached on top of the bore during an actual measurement with the ModFlex coil.

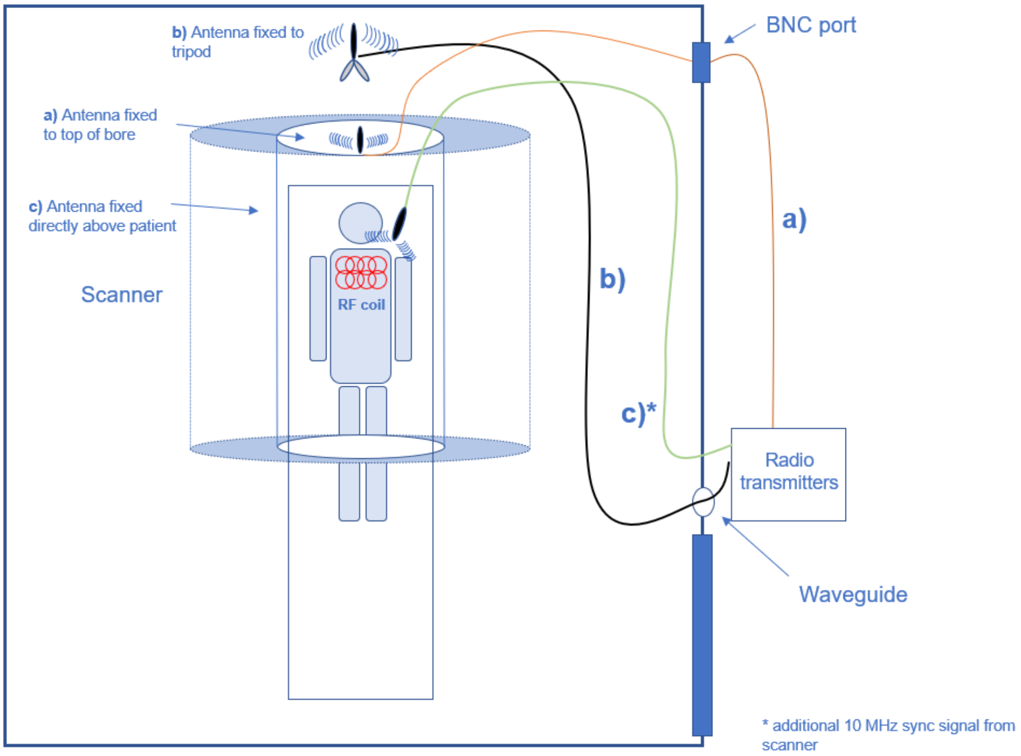

Figure 25: Sketch of the scanner room including the BPT setups **a)** with the antenna attached to the top of the bore **b)** with the antenna fixed to a tripod

Die approbierte gedruckte Originalversion dieser Diplomarbeit ist an der TU Wien Bibliothek verfügbar
The approved original version of this thesis is available in print at TU Wien Bibliothek.
TU WIEN Bibliothek Your knowledge hub

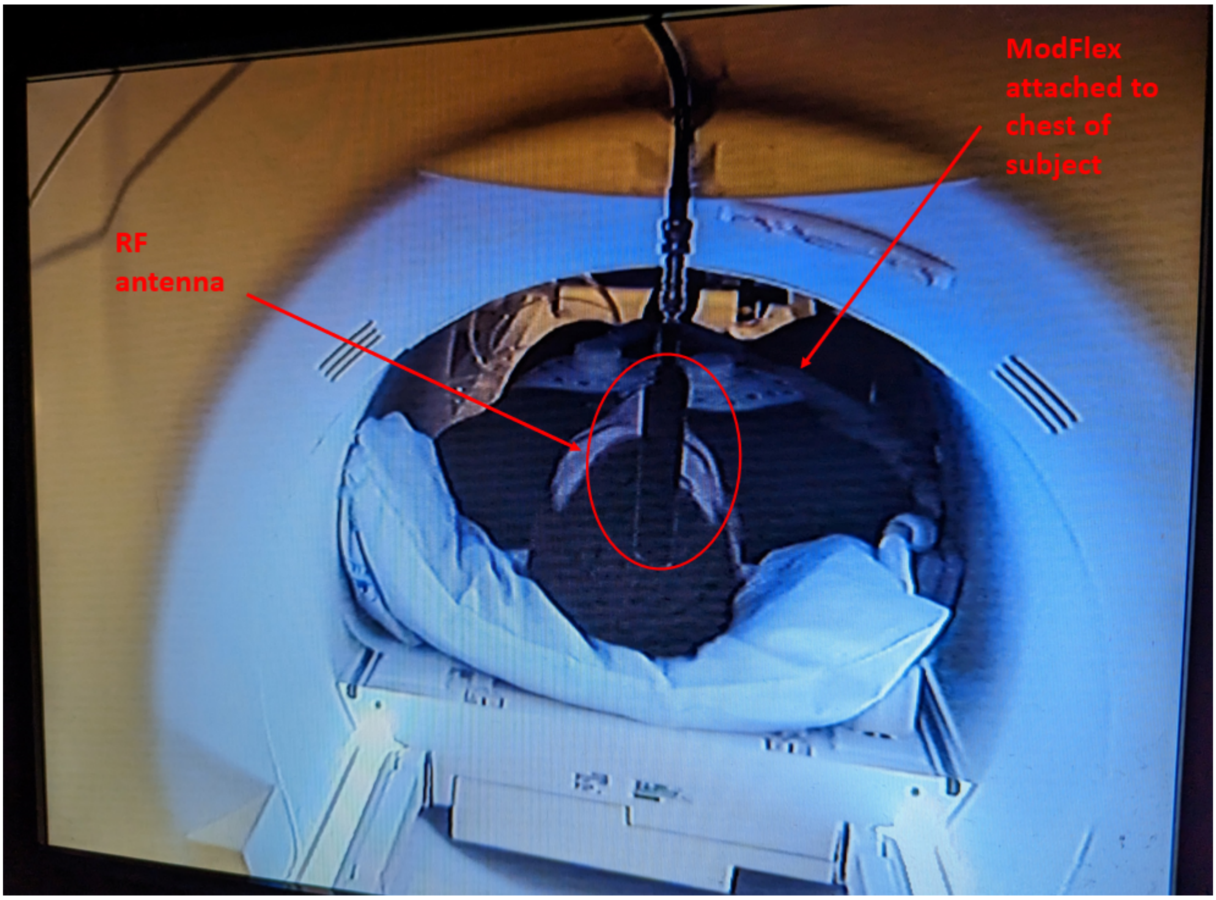

Figure 26: BPT test measurement with patient using setup a) and the ModFlex coil

Sequences and BPT settings

The sequences used for the measurements at the 3T scanner were two different T2 sequences that are clinically relevant for the participating research groups. The first one was a coronal T2w acquisition, that is used for clinical BraCoil measurements of the research group in Vienna and the relevant parameters can be found in tabular 1. The second one was an axial T2w acquisition, created by the IADI research group in Nancy and used since the GRICS algorithm for the reconstruction and motion correction is tailored for axial measurements. The relevant parameters can be found in tabular 2. For the first sequence, the offset Δf of the BPT frequency from the Larmor frequency, that is displayed by the MR scanner after the localizer for each measurement, was set to 41600 kHz, which was 10 kHz off the edge of the oversampling region. This seemed a suitable distance both from the imaging bandwidth so that the BPT peak doesn't interfere with the image, and from the bandwidth edge so that some of the BPT information is not lost. For the second sequence Δf was standardized and set as 0.9 * imaging bandwidth. The power gain of the signals sent by the B210 was first set to a maximum of 89 for the measurements with the ModFlex and to 85 for the measurements with the Body 18

Die approbierte gedruckte Originalversion dieser Diplomarbeit ist an der TU Wien Bibliothek verfügbar
The approved original version of this thesis is available in print at TU Wien Bibliothek.

and BraCoil. This was adjusted by comparing the picked up BPT amplitude with that of the imaging data, to get a comparable amplitude as visible in figure 24.

TR	5510 ms	**turbo factor**	14	**flip angle (°)**	120
TE	150 ms	**acceleration R**	4	**FOV (mm^2)**	376 x 280
BW$_{img}$	344 px * 150 Hz/px = 51.6 kHz	**TA (min:sec)**	02:34	**matrix size**	512 x 406
Δf	41600 kHz	**resolution (mm^3)**	0.6 x 0.6 x 3	**number of slices**	35

Tab.1: MRI pulse sequence parameters of the coronal T2w acquisitions

TR	8940 ms	**turbo factor**	14	**flip angle (°)**	120
TE	144 ms	**acceleration R**	1	**FOV (mm^2)**	337 x 200
BW$_{img}$	320 px * 147 Hz/px = 47 kHz	**TA (min:sec)**	07:46	**matrix size**	540 x 320
Δf	0.9*BW$_{img}$= 42.336 kHz	**resolution (mm^3)**	0.6 x 0.6 x 3	**number of slices**	55

Tab.2: MRI pulse sequence parameters of the axial T2W acquisitions

ModFlex measurements

The first measurements were conducted using a ModFlex coil with two modules, setup a) from figure 25 and the first sequence from tabular 1. Since this was the first test of the BPT setup within the scanner in general, before testing it on a subject the coil was put on a cylindrical phantom and an image was acquired with the BPT frequency tuned to the Larmor frequency without offset. With successful transmission and reception of the BPT signal, it should appear as a line in the middle of the image, demonstrating the functionality of the setup. Figure 27 shows the measurement with the ModFlex on top of the phantom and the BPT antenna fixed to the top of the bore.

Die approbierte gedruckte Originalversion dieser Diplomarbeit ist an der TU Wien Bibliothek verfügbar
The approved original version of this thesis is available in print at TU Wien Bibliothek.
TU WIEN Bibliothek Your knowledge hub

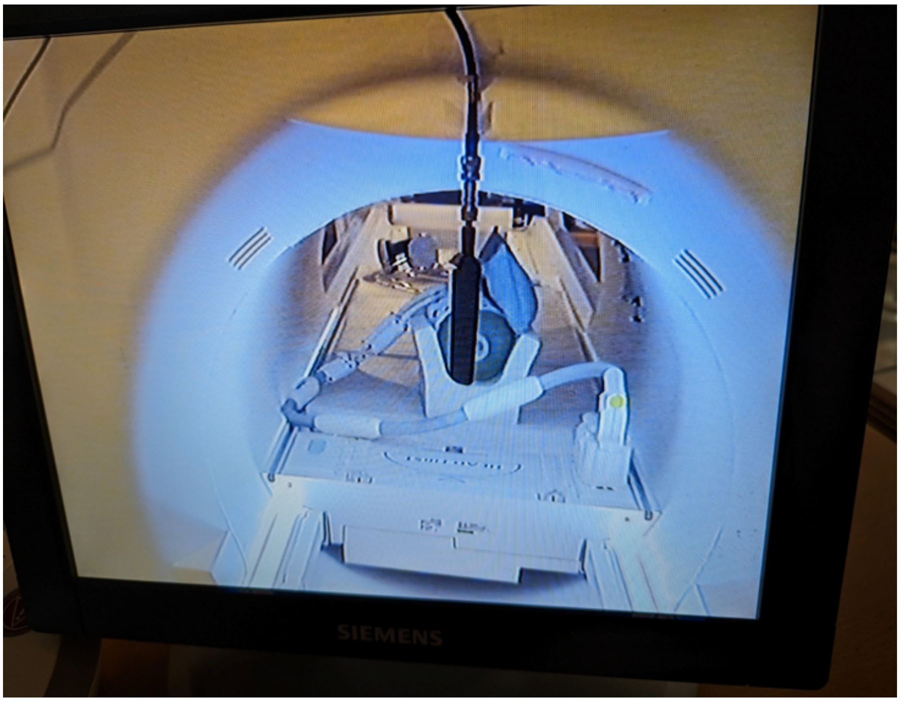

Figure 27: BPT test measurement with phantom using setup a) and the ModFlex coil

After that, a few measurements where the ModFlex was taped to the chest of a subject (m/26 yrs) were taken, a picture of that was already shown in figure 26. To test for sensitivity towards different kinds of motions, three different consecutive measurements were acquired with different instructions for the subject. In the first one just normal breathing was instructed, in the second one constant heavy chest breathing and in the third one rotational upper body motion every 30 seconds.

Body 18 measurements

For the measurements with the Body 18 coil from Siemens, the coil was strapped onto the chest of a subject (f/26 yrs/bra size 75A) and BPT setup b) from figure 25 and sequence 2 from tabular 2 were used. The instructions for the first acquisitions were tailored to test the motion sensitivity, including two phases of 20 seconds breathhold with 20 seconds of normal breathing in between, then a one minute phase of heavy breathing and then two rotational upper body motions with a space of 20 seconds. For the second acquisition just normal breathing throughout the measurement was instructed and this was the first dataset used for reconstruction and motion correction.

BraCoil measurements

The first measurements with the BraCoil were conducted analogous to those with the Body 18 coil, with the same subject (f/26 yrs/bra size 75A), BPT setup b) and the axial sequence 2 from tabular 2. Here three different acquisitions with distinct instructions were taken, one with normal breathing, one with flat abdominal breathing

Die approbierte gedruckte Originalversion dieser Diplomarbeit ist an der TU Wien Bibliothek verfügbar
The approved original version of this thesis is available in print at TU Wien Bibliothek.

to test how the setup reacts to patients with mainly abdominal breathing, and one with heavy chest breathing.

For the final measurements with the BraCoil, the setup was changed to setup c) using the same sequence. To test the influence of the sync signal, the new position above the patient and also the influence of the signal gain, three measurements with the same subject and instructions for normal breathing were acquired. The signal gain was varied in three steps, 80, 85 and 89.

Die approbierte gedruckte Originalversion dieser Diplomarbeit ist an der TU Wien Bibliothek verfügbar
The approved original version of this thesis is available in print at TU Wien Bibliothek.

4 Results

4.1 Wireless motion sensor

In figure 28, the resulting images of the phantom measurements described in 3.1.3 can be seen.

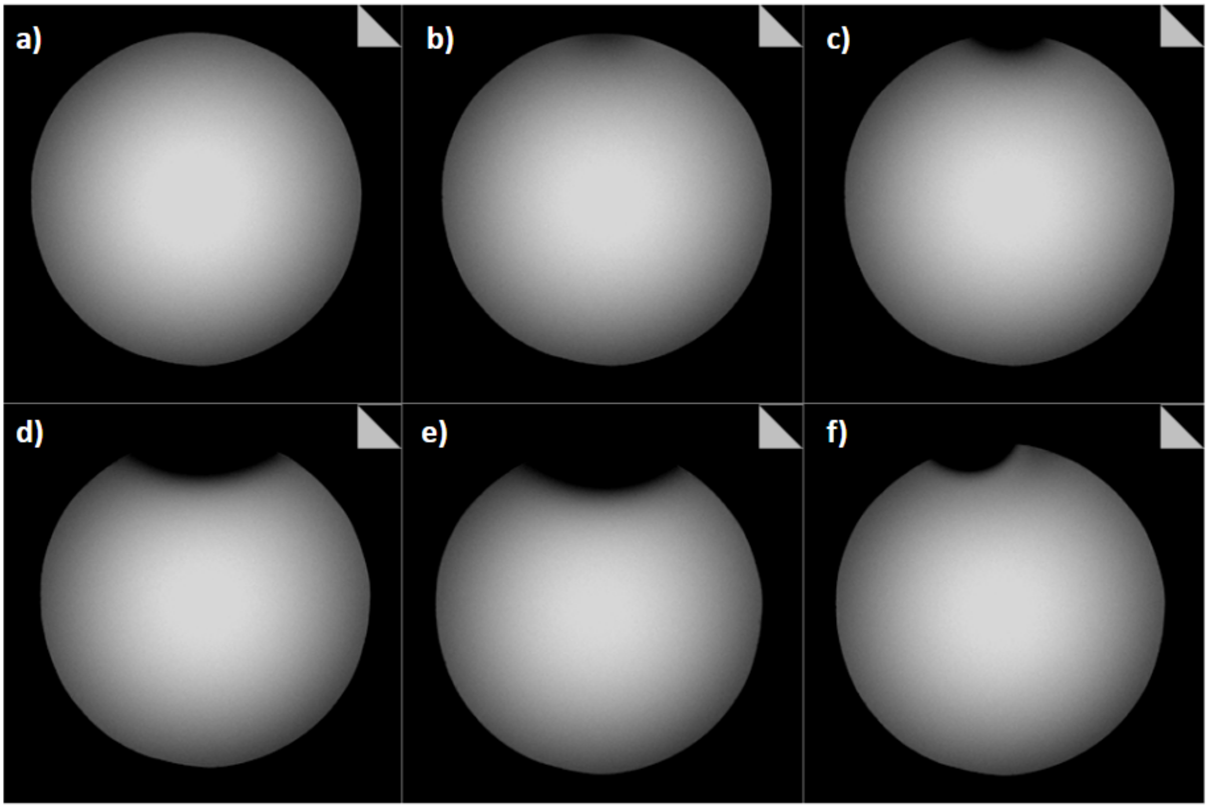

Figure 28: Phantom measurements with varying test objects on top **a)** Reference without cage **b)** Cage only **c)** Cage with battery **d)** Cage with running sensor setup with antenna kept inside **e)** Cage with running sensor setup with antenna reaching outside **f)** Cage with sensor and battery without PCB

As visible the intensity of the image artefact where no signal is picked up close to the top increases as more parts of the sensor setup are added. When the whole running sensor setup is attached to top, a big part of the phantom is cut off. Imagining the distance that the sensor would have to the subject when attached on top of the chest coil, this artefact would very likely appear as well and therefore the setup was not further investigated.

Die approbierte gedruckte Originalversion dieser Diplomarbeit ist an der TU Wien Bibliothek verfügbar
The approved original version of this thesis is available in print at TU Wien Bibliothek.

4.2 Beat-Pilot tone setup

4.2.1 Setup in laboratory

In figure 29 an example frequency spectrum that the VNA outputs around the targeted Larmor frequency is shown, plotting the received amplitude of RF signals in dBm. As visible, exactly at 123 MHz, which is the difference frequency of the incoming RF signals and therefore the set BPT frequency, a clear peak arises ~20 dBm above the baseline. This shows that the setup works as intended and the heterodyne signal mixing at the stage of the preamplifier creates the BPT signal. The peak is found and marked by a peakfinder function in Matlab and its height analyzed with time.

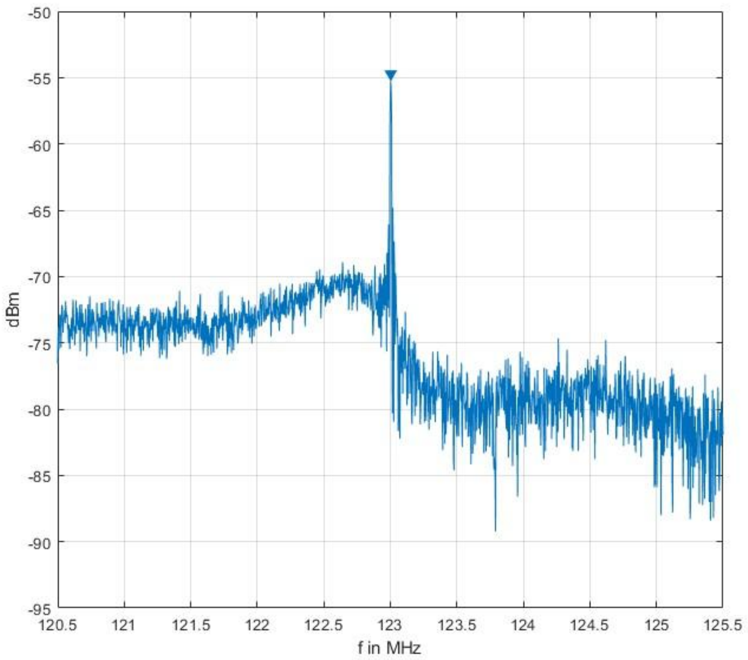

Figure 29: Example of VNA frequency spectrum output of laboratory setup with marked BPT peak

Figure 30 shows the evolution in time of the BPT signal amplitude. The three periods of breathing of the subject indicated by the expected up and down movement of the amplitude can clearly be seen, showing the motion sensitivity of the BPT. The blockiness of the time course stems from the slow refresh rate of the VNA, as mentioned in the materials and methods chapter.

Die approbierte gedruckte Originalversion dieser Diplomarbeit ist an der TU Wien Bibliothek verfügbar
The approved original version of this thesis is available in print at TU Wien Bibliothek.
TU WIEN Bibliothek Your knowledge hub

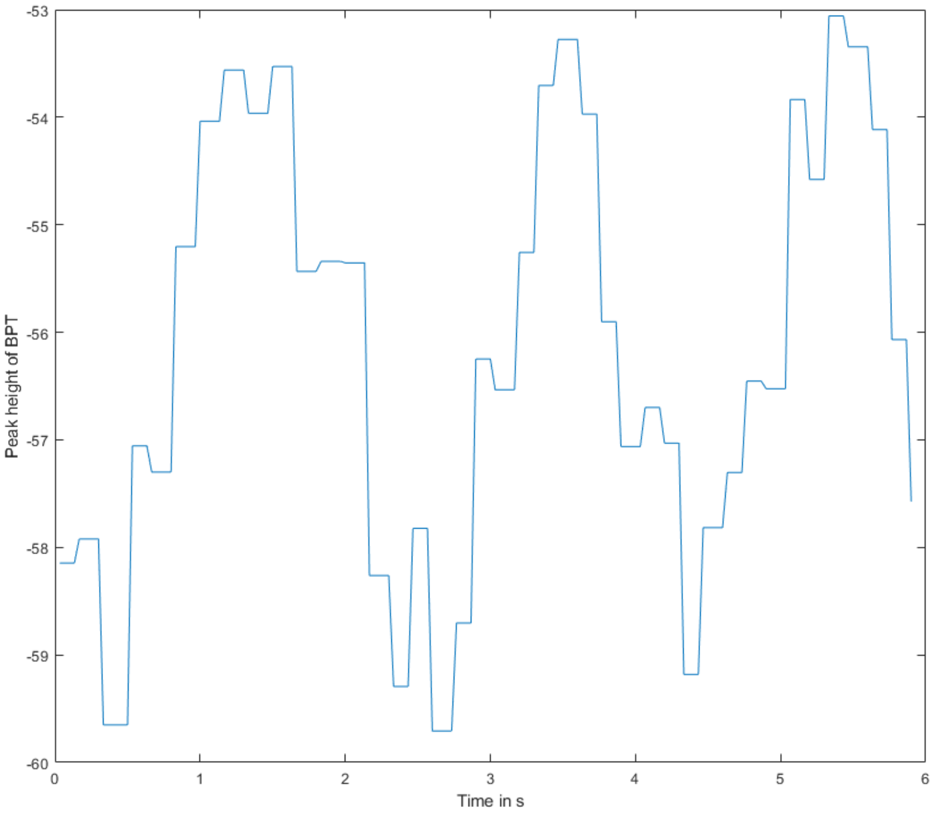

Figure 30: BPT peak amplitude evolution in time

4.2.2 Setup in scanner

4.2.2.1 ModFlex measurements

Test images of phantom and subject

A slice of the low resolution acquisition with the cylindrical phantom where the BPT frequency was set to the Larmor frequency can be seen in figure 31a). As expected a white line appears horizontally in the center, since for every phase encoding step the BPT signal is overlapping the MR signal in the center of the imaging bandwidth. This demonstrates that the setup generally was able to produce a BPT signal at the desired frequency. Figure 31b) shows a slice of the acquisition with the subject with normal breathing, where the BPT frequency was offset into the oversampling region. It can be seen that there are no artefacts anymore that show up due to the BPT signal.

Die approbierte gedruckte Originalversion dieser Diplomarbeit ist an der TU Wien Bibliothek verfügbar
The approved original version of this thesis is available in print at TU Wien Bibliothek.

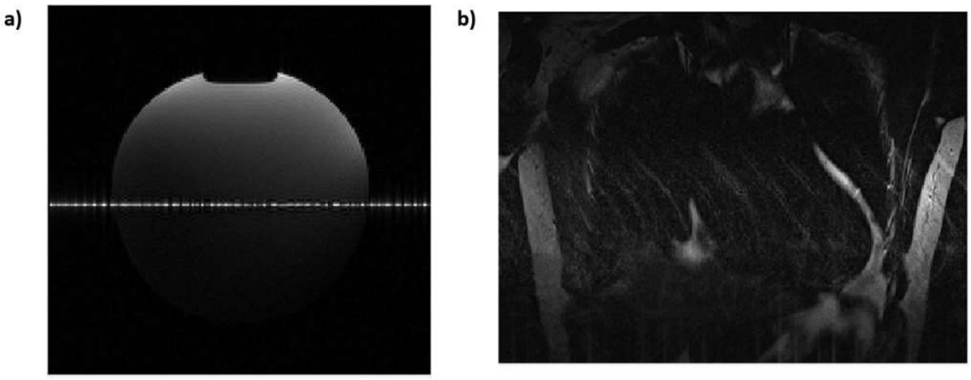

Figure 31: Example slices of ModFlex acquisitions with **a)** phantom and BPT tuned to Larmor frequency **b)** subject and BPT with offset to oversampling region

BPT time-courses

Normal breathing

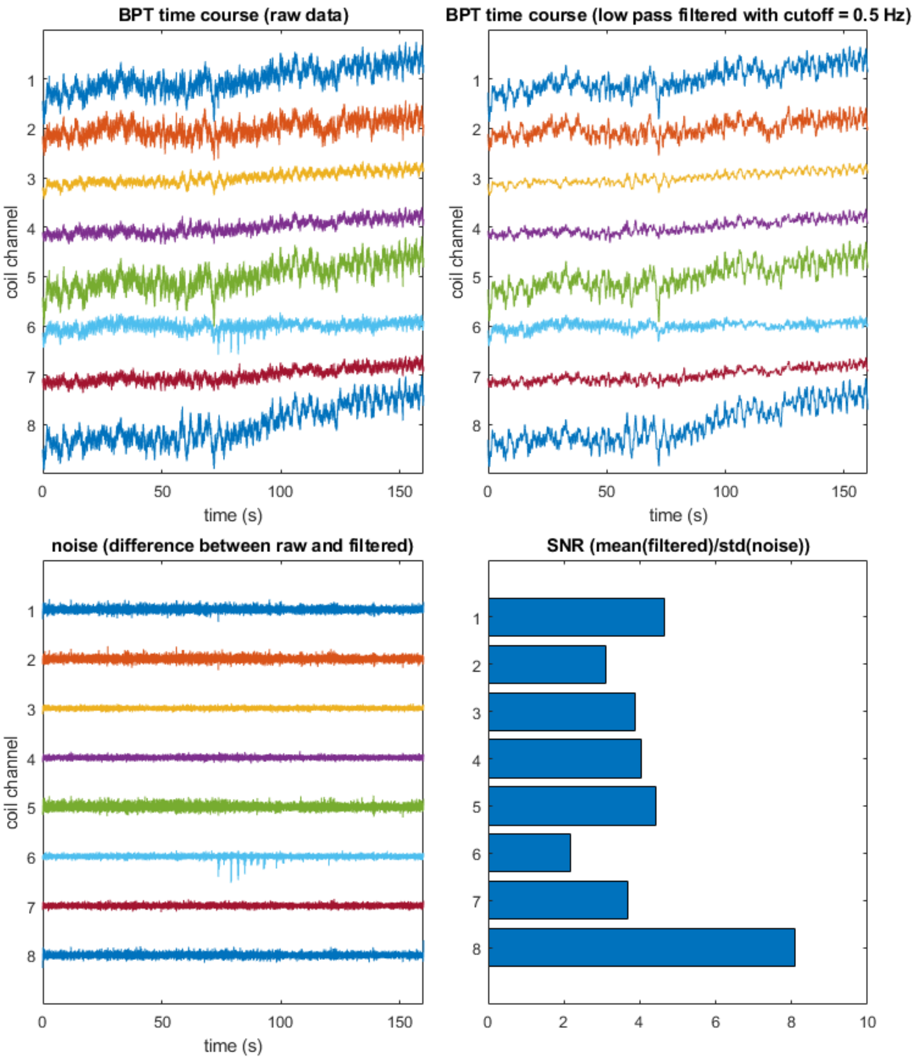

Figure 32: BPT data of normal breathing acquisition with ModFlex including raw time-course, low pass filtered time-course, noise and signal-to-noise ratio

Die approbierte gedruckte Originalversion dieser Diplomarbeit ist an der TU Wien Bibliothek verfügbar
The approved original version of this thesis is available in print at TU Wien Bibliothek.

In figure 32 the BPT time-course plots of the normal breathing acquisition for each of the 8 coils can be seen. The raw data is on the top left, the low pass filtered data on the top right, the filtered out noise on the bottom left and the signal-to-noise ratio on the bottom right. Looking at the filtered time-course, depending on the coil position on the chest the picked up motion signal varies, especially coil 8 and also coil 5 show strong signs of the breathing motion. Other coils seem not to pick up sufficient physiological motion and there seems to be some kind of random fluctuation. The SNR varies accordingly, with a high level of above 8 for coil 8 and around 2-4 for the other coils, which seems sufficient for correction purposes. The filtered out noise seems to be similar for all coils, with some kind of interference signal creating peaks in the middle of the acquisition at coil 6.

Heavy breathing

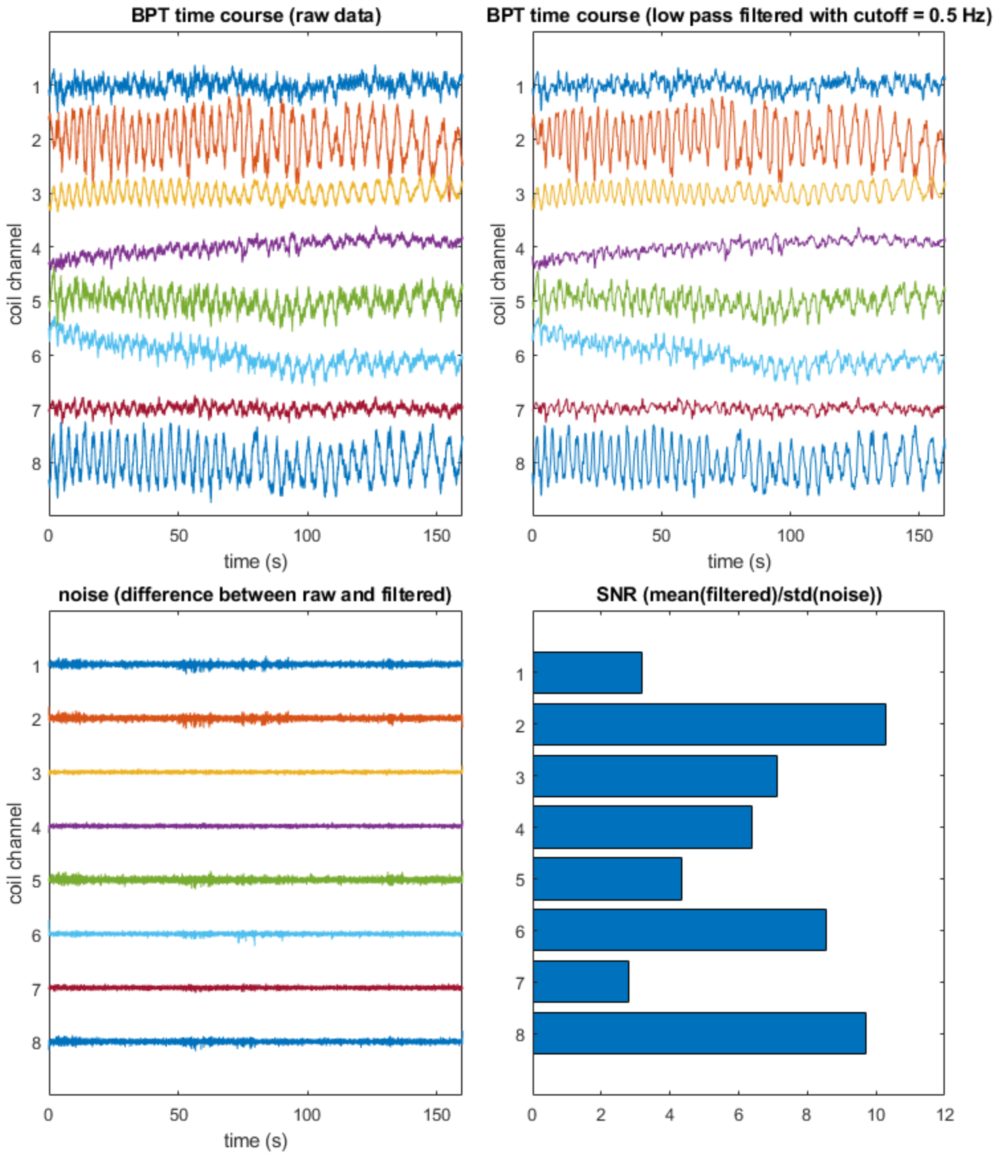

Figure 33: BPT data of heavy breathing acquisition with ModFlex including raw time-course, low pass filtered time-course, noise and signal-to-noise ratio

Die approbierte gedruckte Originalversion dieser Diplomarbeit ist an der TU Wien Bibliothek verfügbar
The approved original version of this thesis is available in print at TU Wien Bibliothek.

In figure 33 the BPT data of the heavy breathing acquisition can be seen and here clearly the breathing motion is picked up by almost all the coils and is a significant amount above the noise level, being also visible in the raw unfiltered data. Also on some coils there seems to be an overlying biphasic signal, for example on coil 5, which could be due to the heartbeat. This could indicate that the improved sensitivity of the BPT signal is even sufficient to measure heart movement, which could be used for reconstruction. The noise looks similarly as in the normal breathing example with no strange behaviour and the SNR reaches levels of even around 10 and is improved for most of the coils.

Body motion

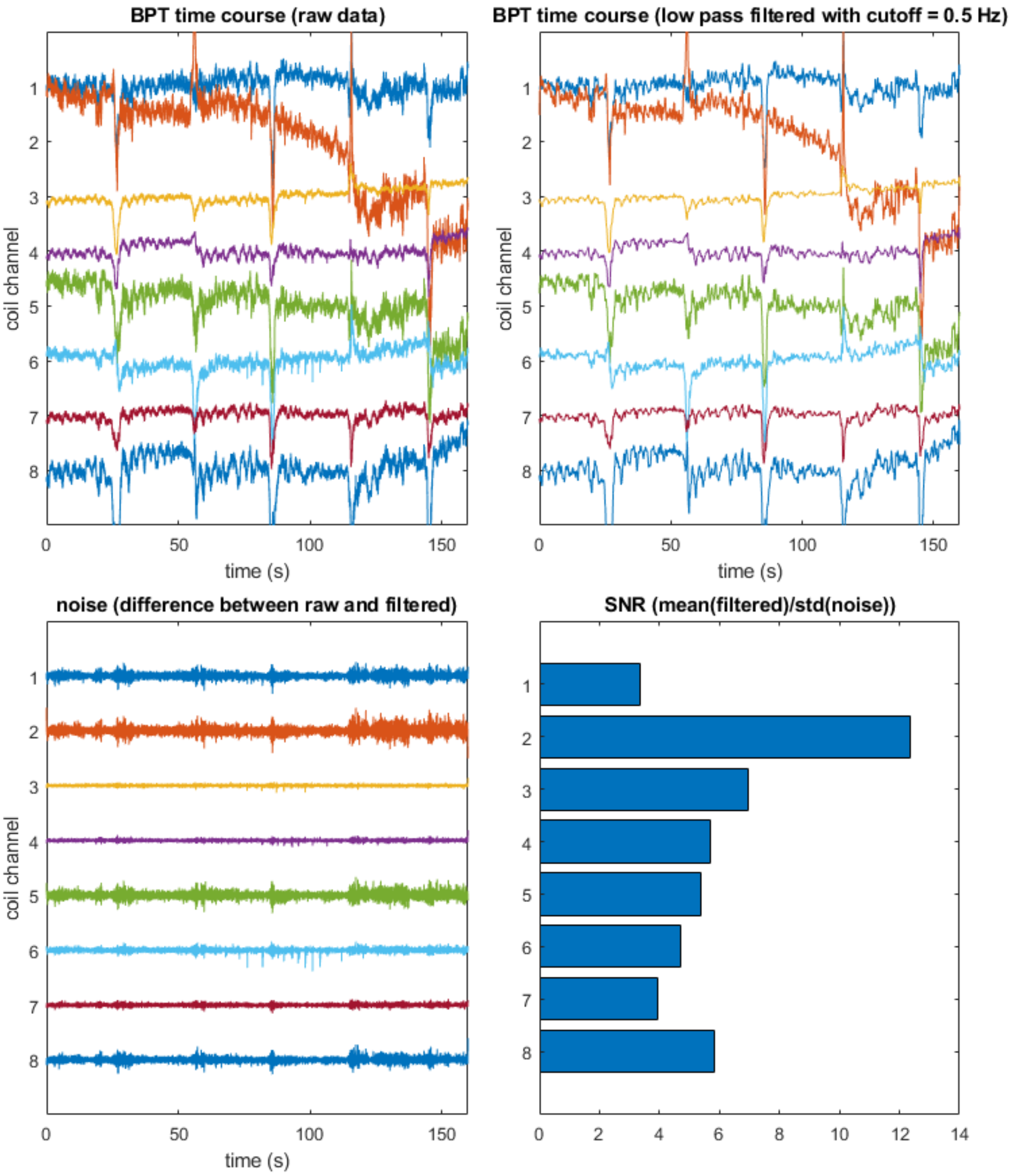

Figure 34: BPT data of body motion acquisition with ModFlex including raw time-course, low pass filtered time-course, noise and signal-to-noise ratio

Die approbierte gedruckte Originalversion dieser Diplomarbeit ist an der TU Wien Bibliothek verfügbar
The approved original version of this thesis is available in print at TU Wien Bibliothek.
TU WIEN Bibliothek Your knowledge hub

In figure 34 the BPT data of the body motion acquisition can be seen and as expected, every 30 seconds when the subject was instructed to move the upper body a peak can be seen in the motion signal. Additionally breathing motion is also visible for some coils.

4.2.2.2 Body 18 measurements

BPT time-courses

Breathhold, heavy breathing and body motion

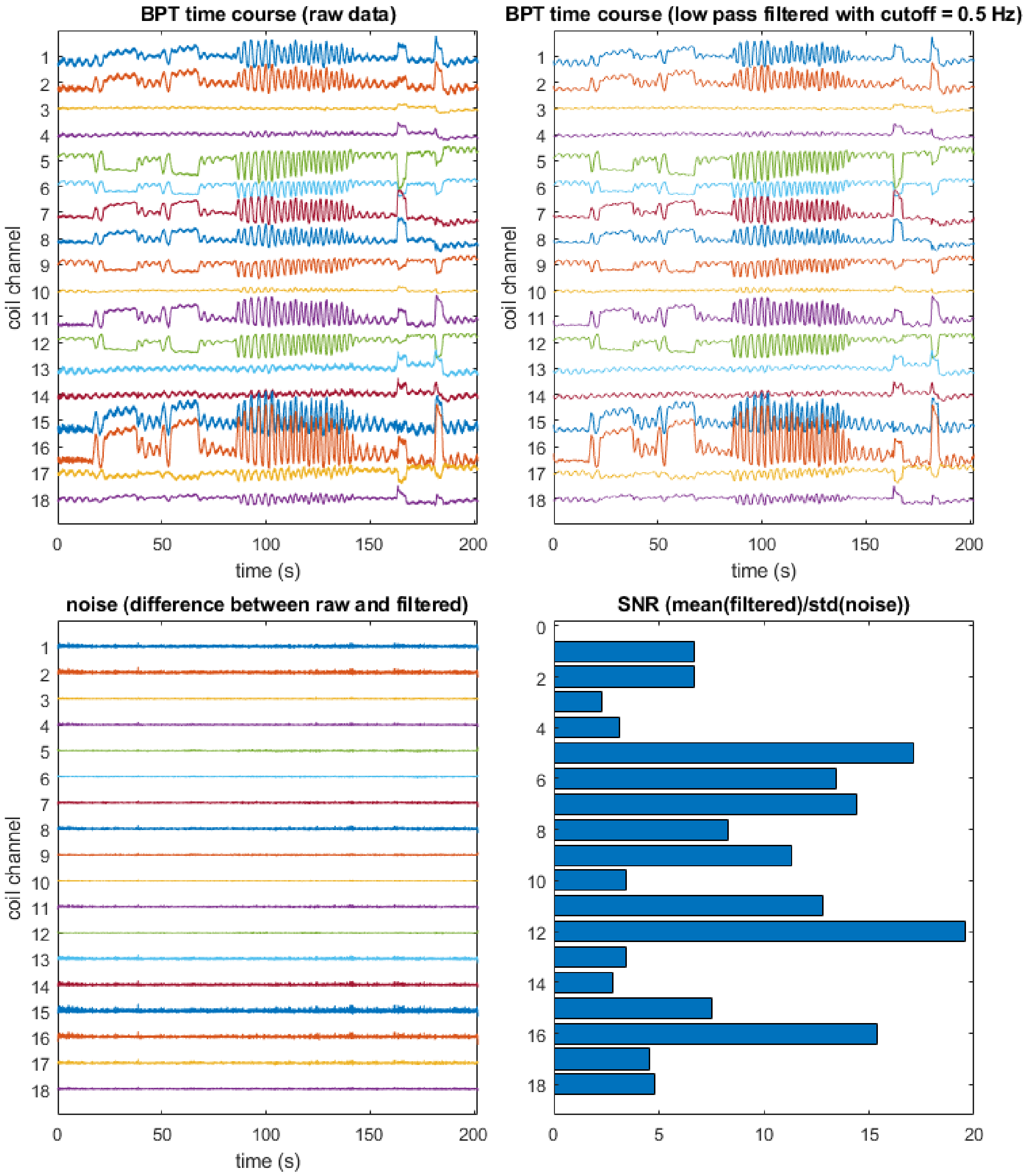

Figure 35: BPT data of breathhold, heavy breathing and body motion acquisition with Body 18 coil including raw time-course, low pass filtered time-course, noise and signal-to-noise ratio

Die approbierte gedruckte Originalversion dieser Diplomarbeit ist an der TU Wien Bibliothek verfügbar
The approved original version of this thesis is available in print at TU Wien Bibliothek.
TU Bibliothek WIEN Your knowledge hub

In figure 35 the BPT data of the acquisition to test the motion sensitivity of the Body 18 setup can be seen. Each of the three phases of motion can clearly be distinguished. The 20 seconds breathhold in the first phase is apparent for most coils, however some coils seem to still pick up some kind of movement. The heavy breathing section is picked up by all coils, aswell as the two upper body motions. This proved that the setup also worked sufficiently for the Body 18 coil and that the noise level is quite low and with this kind of strong motion SNR levels of even over 20 are reachable.

Normal breathing

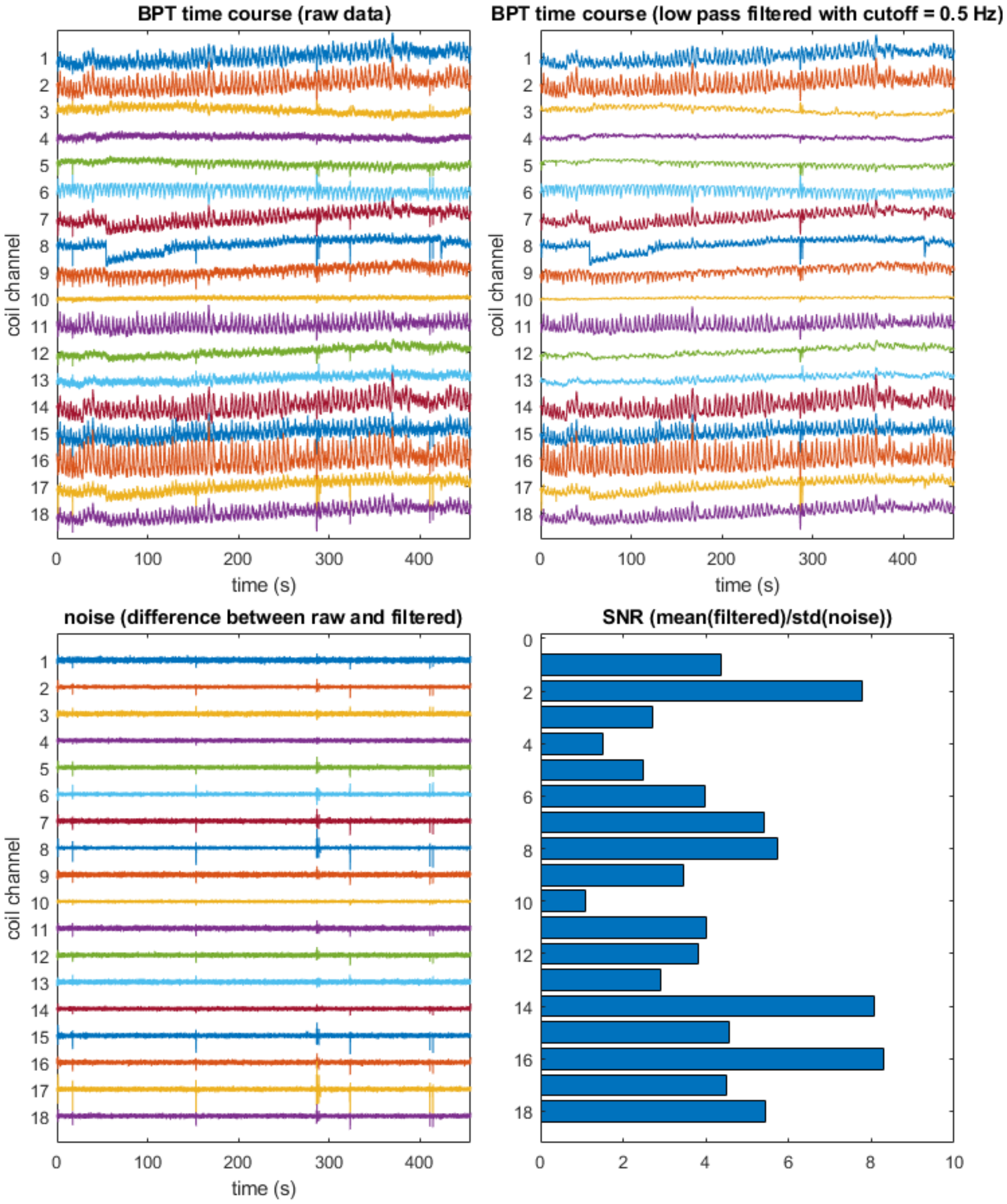

Figure 36: BPT data of normal breathing acquisition with Body 18 coil including raw time-course, low pass filtered time-course, noise and signal-to-noise ratio

Die approbierte gedruckte Originalversion dieser Diplomarbeit ist an der TU Wien Bibliothek verfügbar
The approved original version of this thesis is available in print at TU Wien Bibliothek.
TU Bibliothek WIEN Your knowledge hub

In figure 36 the BPT data of the normal breathing acquisition with the Body 18 can be seen. The breathing motion was successfully captured by most coils with a relatively low noise level, which made this dataset usable as a first test run for the GRICS motion correction.

Reconstructed motion-corrected images

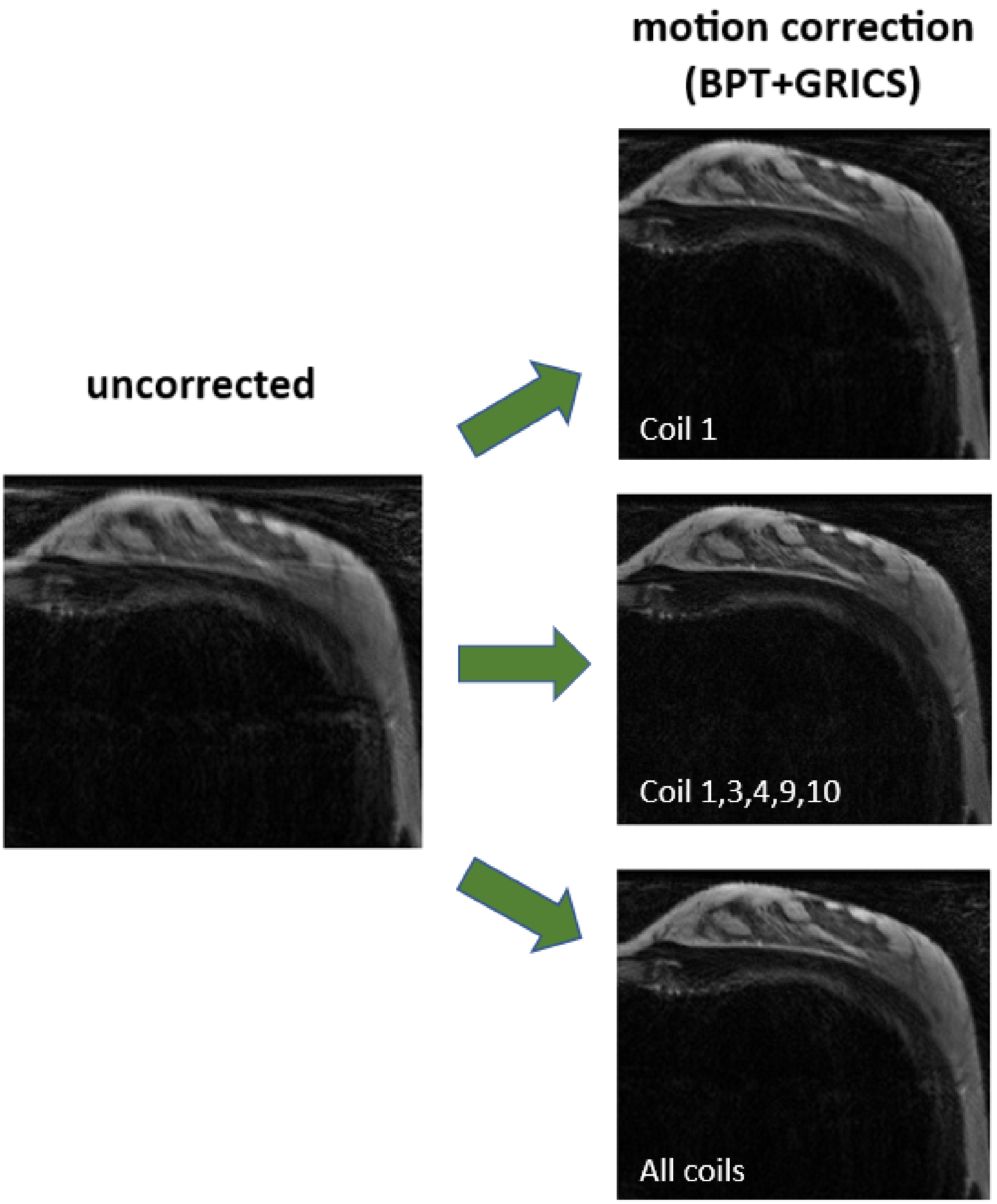

Figure 37: Comparison of uncorrected slice of normal breathing chest acquisition with Body 18 coil and GRICS motion corrected slices using BPT data from different coils

Figure 37 shows the results of the reconstruction and motion correction using the recorded BPT time-courses with the GRICS algorithm. The left side shows an uncorrected section of a slice of the chest measurement with the BraCoil and the

Die approbierte gedruckte Originalversion dieser Diplomarbeit ist an der TU Wien Bibliothek verfügbar
The approved original version of this thesis is available in print at TU Wien Bibliothek.

right side shows three examples, where the BPT time-courses of one coil with the best motion signal, five coils and all the coils were used respectively. Already with the usage of information from one coil, a visible improvement of the image blurring due to breathing artefacts is observable. There is more improvement by using information from more coils, however using all coils seems not to be necessary when comparing it with the image created by using the five best coils. This generally proves that the approach of using BPT+GRICS for motion correction works sufficiently.

4.2.2.3 BraCoil measurements

BPT time-courses from setup b)

Flat abdominal breathing

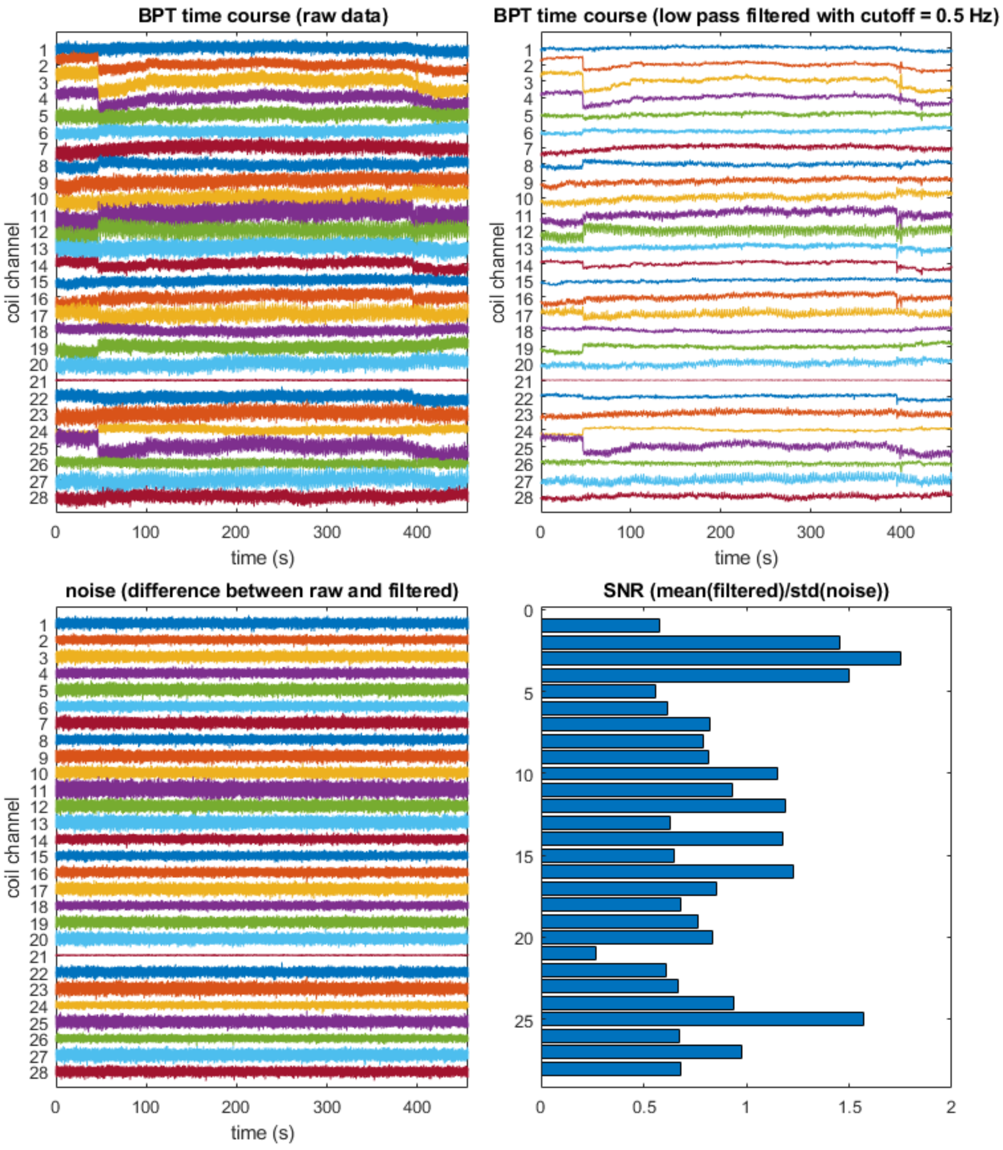

Figure 38: BPT data of flat abdominal acquisition with BraCoil including raw time-course, low pass filtered time-course, noise and signal-to-noise ratio

Die approbierte gedruckte Originalversion dieser Diplomarbeit ist an der TU Wien Bibliothek verfügbar
The approved original version of this thesis is available in print at TU Wien Bibliothek.

Normal breathing

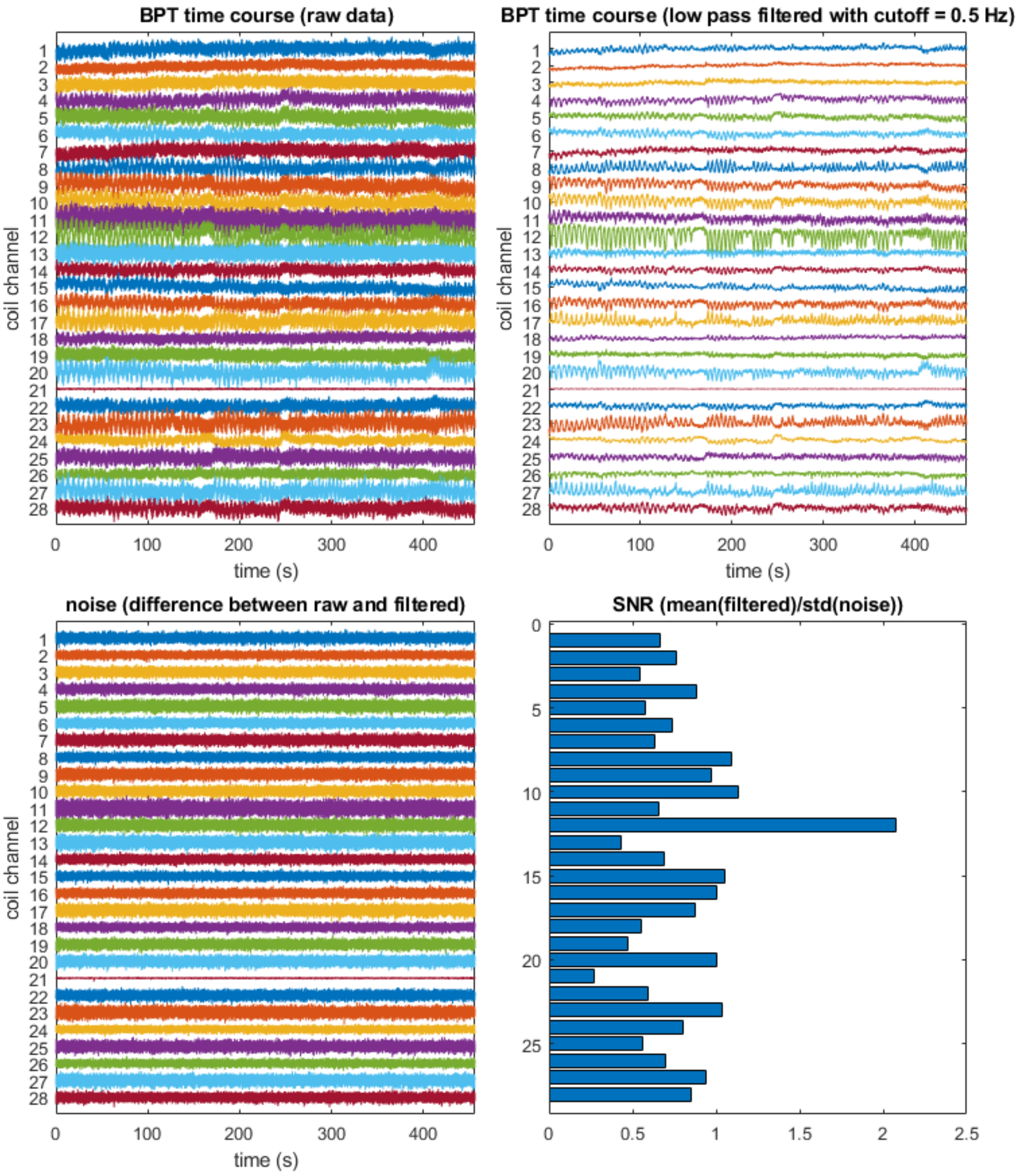

Figure 39: BPT data of normal breathing acquisition with BraCoil including raw time-course, low pass filtered time-course, noise and signal-to-noise ratio

Die approbierte gedruckte Originalversion dieser Diplomarbeit ist an der TU Wien Bibliothek verfügbar
The approved original version of this thesis is available in print at TU Wien Bibliothek.

Heavy breathing

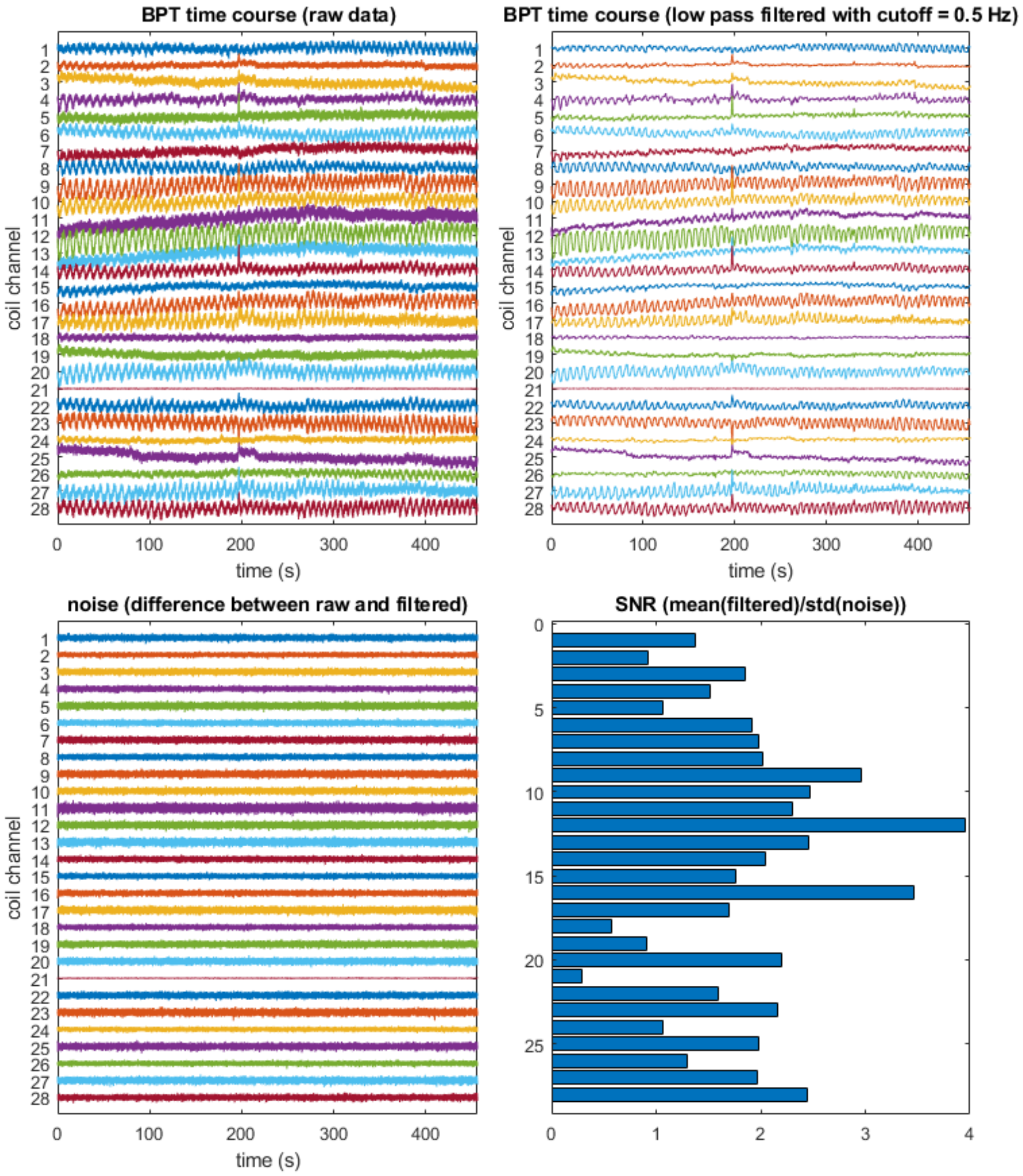

Figure 40: BPT data of heavy breathing acquisition with BraCoil including raw time-course, low pass filtered time-course, noise and signal-to-noise ratio

In figures 38-40 the BPT data for all three acquisitions with the BraCoil, flat abdominal breathing, normal breathing and heavy breathing, are shown. As expected the breathing motion signal gets increasingly stronger per acquisition, correlating with the stronger movement of the coil. For the flat abdominal breathing, no real breathing signal is visible to the eye, only other movement or random signal fluctuations and SNR is quite low. For the normal chest breathing the breathing cycles can be identified, however there are some phases where it goes away, indicating either different subject behaviour or a measurement problem. For the heavy breathing section the breathing cycles can be seen throughout the time-course. This shows

Die approbierte gedruckte Originalversion dieser Diplomarbeit ist an der TU Wien Bibliothek verfügbar
The approved original version of this thesis is available in print at TU Wien Bibliothek.
TU WIEN Bibliothek Your knowledge hub

that the setup in general also works with the BraCoil, and that this data was usable for the GRICS motion correction.

Reconstructed motion-corrected images

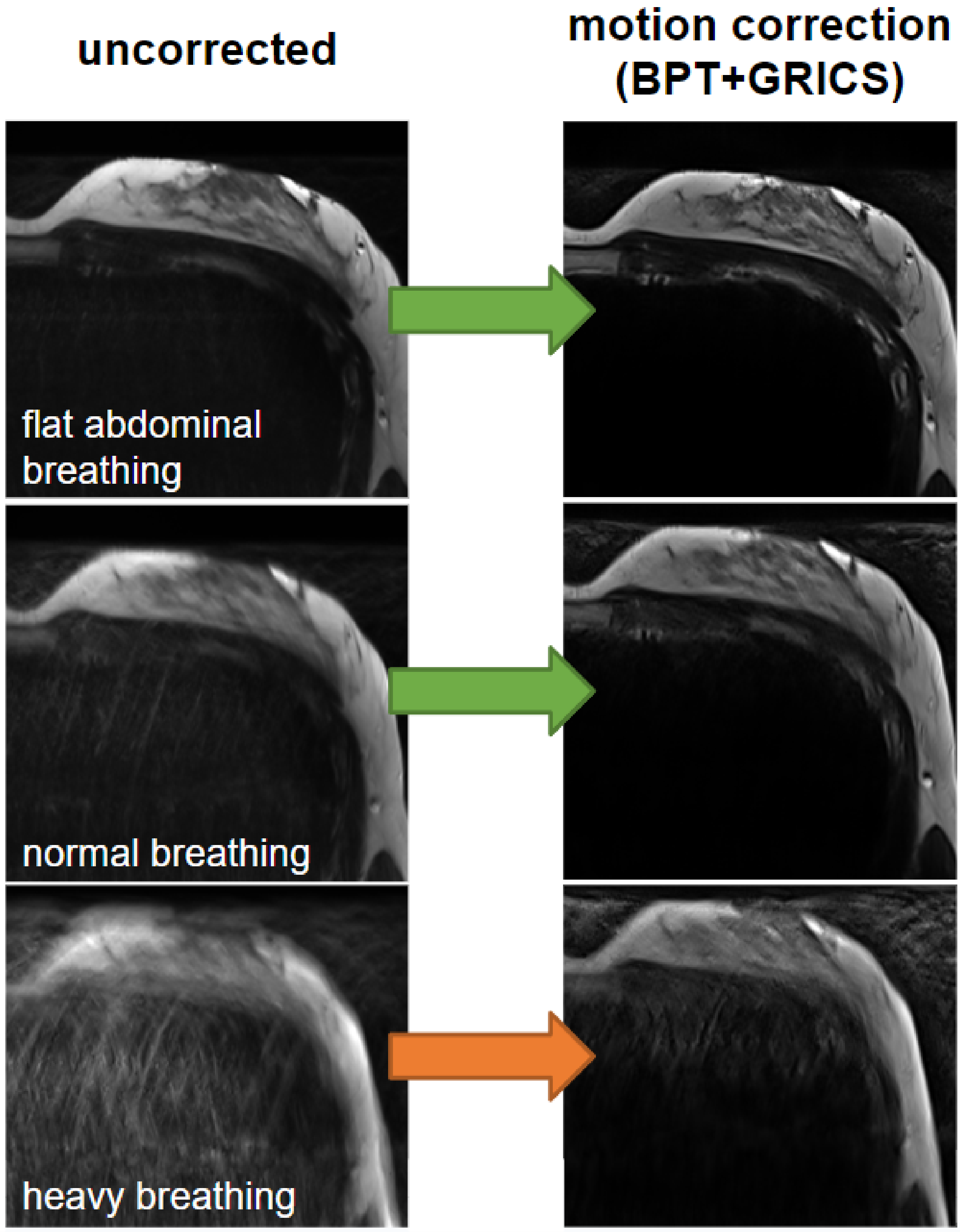

Figure 41: Comparison of uncorrected slices of chest acquisition with BraCoil and GRICS corrected slices using BPT motion data

The results of the motion correction with the BraCoil data is visible in figure 41 for all three acquisitions. Similarly to the results with the Body 18 coil, flat abdominal and

Die approbierte gedruckte Originalversion dieser Diplomarbeit ist an der TU Wien Bibliothek verfügbar
The approved original version of this thesis is available in print at TU Wien Bibliothek.
TU Bibliothek WIEN Your knowledge hub

normal breathing artefacts resulting in image blurring could be visibly reduced and a sharper image with improved visibility of tissue structure was achieved. Even for the heavy breathing acquisition, where in the uncorrected image due to the strong breathing artefacts no real structure was visible the general shape of the tissue was recoverable.

BPT time-courses from setup c)

Gain=80

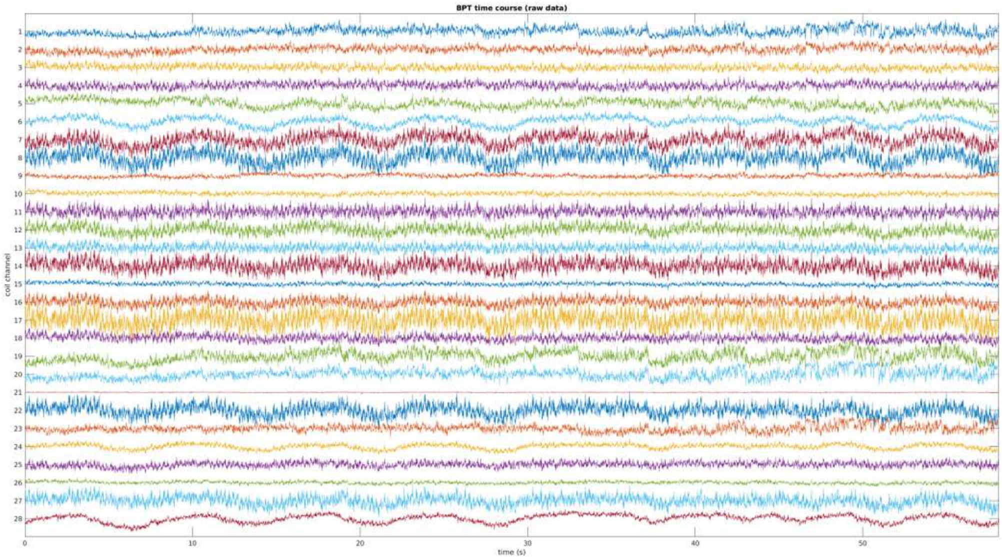

Figure 42: Raw BPT time-course of normal breathing acquisition with BraCoil and setup c) with a signal gain 80

Gain=85

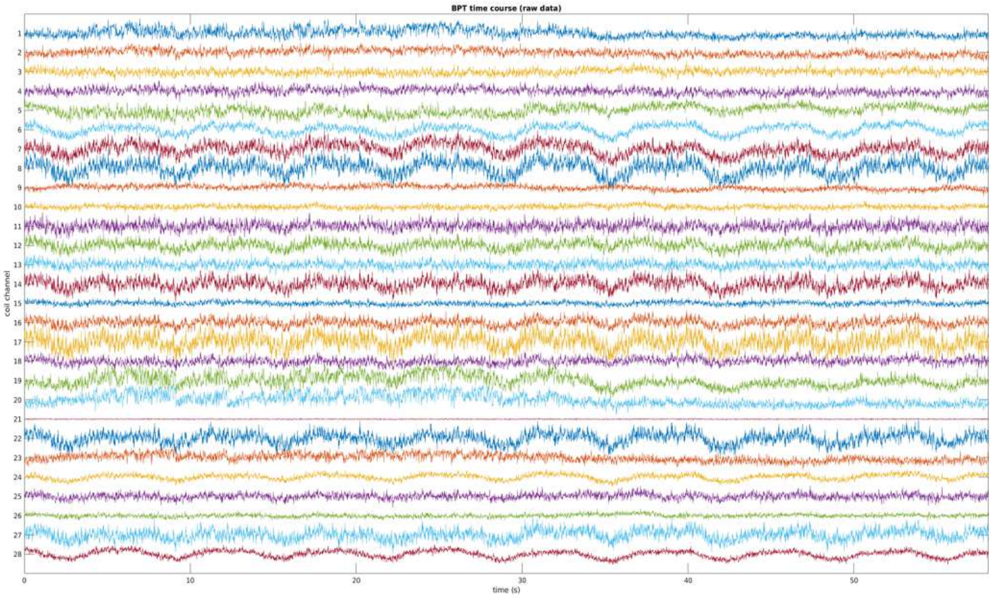

Figure 43: Raw BPT time-course of normal breathing acquisition with BraCoil and setup c) with a signal gain 85

Die approbierte gedruckte Originalversion dieser Diplomarbeit ist an der TU Wien Bibliothek verfügbar
The approved original version of this thesis is available in print at TU Wien Bibliothek.

Gain=89

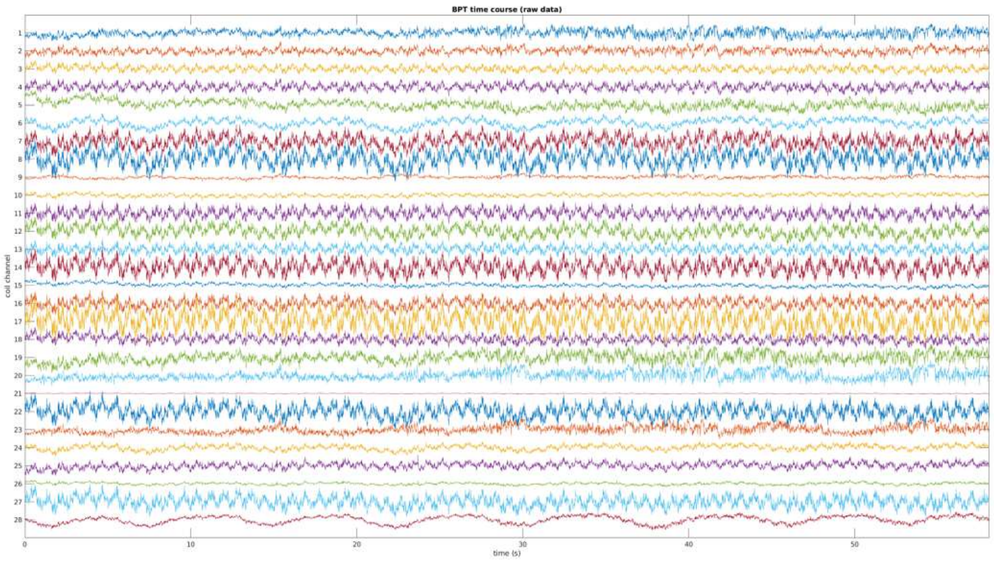

Figure 44: Raw BPT time-course of normal breathing acquisition with BraCoil and setup c) with a signal gain of 89

In figures 42-44 the results from the measurements using the setup with the antenna directly above the patient, using cable traps and the sync signal can be seen. Comparing them to the normal breathing acquisition in figure 39, a significant improvement in signal quality is visible, indicating that setup c) eliminates some interferences from outside. Increasing the signal gain also seems to bring an improvement to the signal, with the heartbeat being more and more visible with higher gain. In figure 44 with the gain being 89 the biphasic signal of the heartbeat is clearly visible for almost all channels.

Die approbierte gedruckte Originalversion dieser Diplomarbeit ist an der TU Wien Bibliothek verfügbar
The approved original version of this thesis is available in print at TU Wien Bibliothek.
TU WIEN Bibliothek Your knowledge hub

5 Summary

5.1 Discussion and conclusion

The results of this thesis suggest that the approach with the MR compatible wireless motion sensor was not a promising strategy for this kind of motion detection, since it caused noticeable artefacts already while using a phantom. This ruled out further tests at least with this specific hardware. Changing the sensor hardware while ensuring non-magnetic behaviour might have been a possible solution to this kind of problem, but the tests with the BPT setup showed that a more elegant approach is possible. Since there is less additional hardware required and it could be applied independently of the coil used for differing measurements, it was decided to go into this direction.

That the BPT mechanism in general works with the given coils and preamplifiers was proven with the setup in the laboratory, showing that the BPT difference signal of the two frequencies could be successfully picked up and measured via the network analyzer. Furthermore the motion sensitivity of the BPT amplitude could be shown via a breathing subject measurement, where the amplitude behaviour showed the exact dynamics of the breathing instructions. This motivated the application within the scanner while using the target coil arrays. The first measurements in the scanner using the ModFlex as the coil and a subject with different breathing and motion instructions showed that the movement could successfully be retrieved by analyzing the BPT signal within the raw scanner data. For the normal breathing sequence the signal was not strong enough for all coils, but in general breathing, heartbeat and upper body motion was visible for most coils especially when the subject was instructed to breathe heavily.

In order to improve the quality of the recorded BPT motion signals, three different scanner setups with different locations of the antenna were tested throughout the process. In the final setup, the coaxial cable was led through the waveguide next to the entrance, shielded with cable traps and the antenna was fixed inside of the bore directly above the patient. Also a 10 MHz sync signal provided by the scanner was applied to the signal generators, synchronizing the two BPT signals. This setup showed to eliminate interference signals that were occurring before with the other approaches.

To test if these recorded motion signals could be sufficient for motion correction, measurement with the designated chest-coils BraCoil and Body 18 were conducted with an axial T2 sequence that was suitable for the GRICS algorithm. For both coils for the acquisitions including normal chest and flat abdominal breathing the

Die approbierte gedruckte Originalversion dieser Diplomarbeit ist an der TU Wien Bibliothek verfügbar
The approved original version of this thesis is available in print at TU Wien Bibliothek.
TU WIEN Bibliothek Your knowledge hub

reconstruction and motion correction using GRICS+BPT was able to provide noticeable improvement when it comes to image blurring artefacts.

This proves that the combination of these two techniques is a promising approach for motion correction in free breathing supine breast MRI. Especially the advantages that the BPT setup can be combined with any coil or sequence renders it an interesting approach for clinical applications in the future.

5.2 Outlook

Even if this base setup already delivers satisfying results, several improvements are still imaginable that could be subject of further research. On the one hand, methodical automation is an issue that has to be handled when it comes to clinical application. As of right now, the frequency offset at the signal generators is typed in by hand tailored to the used sequence and the transmission is controlled using a different computer. Establishing communication between the scanner controls and the signal generators will become necessary, in order to automatically start the signal transmission with the right frequencies simultaneously to the start of the sequence. On the other hand, a more in depth analysis of the resulting BPT signal and how it reacts to possible interferences would be required. The final setup using the cable traps and sync signal seems to eliminate most of the interferences, yet it has to still be investigated if this is stable over time. Finally, another idea for the future is to transmit more than two signals within different frequency ranges, in order to generate multiple BPT signals that are sensitive towards different motions, e.g. one for breathing and one for heart motion. Many of these investigations are already planned for the future.

Die approbierte gedruckte Originalversion dieser Diplomarbeit ist an der TU Wien Bibliothek verfügbar
The approved original version of this thesis is available in print at TU Wien Bibliothek.

6 References

[1] M. Zaitsev, J. Maclaren, and M. Herbst, “Motion artifacts in MRI: A complex problem with many partial solutions,” *J. Magn. Reson. Imaging*, vol. 42, no. 4, pp. 887–901, Oct. 2015.

[2] R. Gerami *et al.*, “A literature review on the imaging methods for breast cancer,” *Int. J. Physiol. Pathophysiol. Pharmacol.*, vol. 14, no. 3, pp. 171–176, Jun. 2022.

[3] M. Obermann *et al.*, “Panoramic Magnetic Resonance Imaging of the Breast With a Wearable Coil Vest,” *Invest. Radiol.*, May 2023, doi: 10.1097/RLI.0000000000000991.

[4] R. W. Brown, Y.-C. N. Cheng, E. Mark Haacke, M. R. Thompson, and R. Venkatesan, *Magnetic Resonance Imaging: Physical Principles and Sequence Design*. John Wiley & Sons, 2014.

[5] M. T. Vlaardingerbroek and J. A. den Boer, “Magnetic Resonance Imaging.” 2003. doi: 10.1007/978-3-662-05252-5.

[6] F. Bloch, W. W. Hansen, and M. Packard, “The Nuclear Induction Experiment,” *Physical Review*, vol. 70, no. 7–8. pp. 474–485, 1946. doi: 10.1103/physrev.70.474.

[7] E. M. Purcell, H. C. Torrey, and R. V. Pound, “Resonance Absorption by Nuclear Magnetic Moments in a Solid,” *Physical Review*, vol. 69, no. 1–2. pp. 37–38, 1946. doi: 10.1103/physrev.69.37.

[8] V. Kuperman and V. L. Kuperman, *Magnetic Resonance Imaging: Physical Principles and Applications*. Academic Press, 2000.

[9] P. Sprawls, *Magnetic Resonance Imaging: Principles, Methods, and Techniques*. Medical Physics Publishing Corporation, 2000.

[10] T. Twellmann, *Data Driven Analysis of Dynamic Contrast Enhanced Magnetic Resonance Imaging Data in Breast Cancer Diagnosis*. 2005.

[11] C. B. Paschal and H. D. Morris, “K-space in the clinic,” *J. Magn. Reson. Imaging*, vol. 19, no. 2, pp. 145–159, Feb. 2004.

[12] W. Demtröder, *Experimentalphysik 2: Elektrizität und Optik*. Springer-Verlag, 2018.

[13] B. Gruber, M. Froeling, T. Leiner, and D. W. J. Klomp, “RF coils: A practical guide for nonphysicists,” *J. Magn. Reson. Imaging*, vol. 48, no. 3, pp. 590–604, Jun. 2018.

[14] A. Stadler, W. Schima, A. Ba-Ssalamah, J. Kettenbach, and E. Eisenhuber, “Artifacts in body MR imaging: their appearance and how to eliminate them,” *Eur. Radiol.*, vol. 17, no. 5, pp. 1242–1255, May 2007.

[15] T. Li and S. A. Mirowitz, “Comparative study of fast MR imaging: quantitative analysis on image quality and efficiency among various time frames and contrast behaviors,” *Magn. Reson. Imaging*, vol. 20, no. 6, pp. 471–478, Jul. 2002.

[16] G. E. Sarty, “Single TrAjectory Radial (STAR) imaging,” *Magn. Reson. Med.*, vol. 51, no. 3, pp. 445–451, Mar. 2004.

[17] R. L. Ehman and J. P. Felmlee, “Adaptive technique for high-definition MR imaging of moving structures,” *Radiology*, vol. 173, no. 1, pp. 255–263, Oct. 1989.

[18] M. Tilli, M. Paulasto-Kröckel, M. Petzold, H. Theuss, T. Motooka, and V. Lindroos, *Handbook of Silicon Based MEMS Materials and Technologies*. Elsevier, 2020.

[19] Pancoast L., Brantner D., Wiggins R., Walczyk J., Brown R., “Wireless Body Sensor Data Acquisition Platform for Motion Tracking,” in *ISMRM*, Center for Advanced Imaging Innovation and Research (CAI2R), Department of Radiology, New York University Grossman School of Medicine, 2021.

[20] Speier P, Rehner R, “PT-nav: a novel respiratory navigation method for continuous acquisitions based modulation of a pilot tone in the MR-receiver,” in *Proceedings from the European Society for Magnetic Resonance in Medicine and Biology*, 2015, p. 128.

[21] J. Ludwig, P. Speier, F. Seifert, T. Schaeffter, and C. Kolbitsch, “Pilot tone-based motion correction for prospective respiratory compensated cardiac cine MRI,” *Magn. Reson. Med.*, vol. 85, no. 5, pp. 2403–2416, May 2021.

[22] M. B. L. Falcão *et al.*, “Pilot tone navigation for respiratory and cardiac motion-resolved free-running 5D flow MRI,” *Magn. Reson. Med.*, vol. 87, no. 2, pp. 718–732, Feb. 2022.

TU WIEN Bibliothek Your knowledge hub
Die approbierte gedruckte Originalversion dieser Diplomarbeit ist an der TU Wien Bibliothek verfügbar
The approved original version of this thesis is available in print at TU Wien Bibliothek.

[23] E. Solomon *et al.*, “Free-breathing radial imaging using a pilot-tone radiofrequency transmitter for detection of respiratory motion,” *Magn. Reson. Med.*, vol. 85, no. 5, pp. 2672–2685, May 2021.

[24] D. Buikman, T. Helzel, and P. Röschmann, “The rf coil as a sensitive motion detector for magnetic resonance imaging,” *Magn. Reson. Imaging*, vol. 6, no. 3, pp. 281–289, May-Jun 1988.

[25] Anand S, Lustig M, “Beat Pilot Tone: Exploiting Preamplifier Intermodulation of UHF/SHF RF for Improved Motion Sensitivity over Pilot Tone Navigators,” in *ISMRM*, Electrical Engineering and Computer Sciences, University of California, 2021.

[26] Wikimedia Foundation, “Heterodyne,” *Wikipedia*. https://en.wikipedia.org/wiki/Heterodyne#Mixer (accessed Jul. 20, 2023).

[27] G. J. Verbiest and M. J. Rost, “Beating beats mixing in heterodyne detection schemes,” *Nat. Commun.*, vol. 6, p. 6444, Mar. 2015.

[28] Lamar-Bruno K., Anand S., Lustig M., “Cardiac and Respiratory-Resolved Image Reconstruction with the Beat Pilot Tone,” in *Proc ISMRM #4446 (2022)*,

[29] C. Forman, M. Aksoy, J. Hornegger, and R. Bammer, “Self-encoded marker for optical prospective head motion correction in MRI,” *Med. Image Anal.*, vol. 15, no. 5, pp. 708–719, Oct. 2011.

[30] A. Z. Kyme, M. Aksoy, D. L. Henry, R. Bammer, and J. Maclaren, “Marker-free optical stereo motion tracking for in-bore MRI and PET-MRI application,” *Med. Phys.*, vol. 47, no. 8, pp. 3321–3331, Aug. 2020.

[31] A. Gholipour, M. Polak, A. van der Kouwe, E. Nevo, and S. K. Warfield, “Motion-robust MRI through real-time motion tracking and retrospective super-resolution volume reconstruction,” *Conf. Proc. IEEE Eng. Med. Biol. Soc.*, vol. 2011, pp. 5722–5725, 2011.

[32] D. Maziero, C. Rondinoni, T. Marins, V. A. Stenger, and T. Ernst, “Prospective motion correction of fMRI: Improving the quality of resting state data affected by large head motion,” *Neuroimage*, vol. 212, p. 116594, May 2020.

[33] F. Odille, P.-A. Vuissoz, P.-Y. Marie, and J. Felblinger, “Generalized reconstruction by inversion of coupled systems (GRICS) applied to free-breathing MRI,” *Magn. Reson. Med.*, vol. 60, no. 1, pp. 146–157, Jul. 2008.

[34] STMicroelectronics, “LIS331HH: MEMS digital output motion sensor ultra low-power high full-scale 3-axes ‘nano’ accelerometer,” *Doc ID 16366 Rev 1 Datasheet*, Oct. 2009, Accessed: Mar. 05, 2023. [Online]. Available: https://www.micro-semiconductor.com/datasheet/67-LIS331HHTR.pdf

[35] G. L. Pollack and D. R. Stump, *Electromagnetism*. Addison-Wesley, 2002.

[36] L. Nohava, M. Obermann, R. Frass-Kriegl, O. Soanca, and E. Laistler, “A modular system of flexible receive-only coil arrays for 3 T Magnetic Resonance Imaging,” *Z. Med. Phys.*, May 2023, doi: 10.1016/j.zemedi.2023.05.002.

[37] J. Near, “mapVBVD Documentation,” *Github*. https://github.com/CIC-methods/FID-A/tree/master/inputOutput/mapVBVD (accessed Aug. 03, 2023).

Die approbierte gedruckte Originalversion dieser Diplomarbeit ist an der TU Wien Bibliothek verfügbar
The approved original version of this thesis is available in print at TU Wien Bibliothek.
TU WIEN Bibliothek Your knowledge hub

7 Appendix

bpt_analyze Matlab script

```
%% bpt analyze
% this script reads Siemens MR raw data that has been acquired concurrently
% with a beat pilot tone (BPT) signal and
% TO DO:
% - read bandwidth from header and calculate BPT offset from Larmor frequency
% - auto-detect BPT peakrange

basedir=''; % set base directory
resultdir=[basedir,'results/'];
saveresults=1;

%% define data set
    raw=''; % path of raw file
    mid='';
    BPT.info.peakrange=78:82;    % location of BPT peak

%% read raw data
    kspaceStruct = mapVBVD(raw); %'removeOS'
    if (iscell(kspaceStruct))
        kspaceStruct = kspaceStruct{1,end};
    end
    data = fftshift(ifft(ifftshift(kspaceStruct.image.unsorted(),1),[],1),1); %only
    ifft applied. ifftshift+fftshift is for data reordering (center freq).
    tmp=kspaceStruct.image.timestamp;

%% fill BPT struct with metadata
    BPT.time.t=(tmp-min(tmp))*2.5e-3;          %time axis for plotting BPT.time
    BPT.info.timepoints=length(BPT.time.t);   %number of timepoints
    BPT.info.dt=max(BPT.time.t)/BPT.info.timepoints;    %time resolution
    BPT.info.df=1/max(BPT.time.t);             %frequency resolution
    BPT.info.fs=1/BPT.info.dt;                 %sampling frequency
    BPT.info.Fmax=BPT.info.fs/2;               %maximum frequency (Nyquist)
    BPT.info.dataset=[basedir,raw];            %file name and directory of original
    data
    BPT.info.nchannels=size(data,2);           %number of channels
    BPT.info.lowpass_cutoff=0.5;% Hz

    %% extract and filter bpt data
    BPT.time.orig = squeeze(abs(sum(data(BPT.info.peakrange,:,:),1)));
    BPT.time.orig = BPT.time.orig-mean(BPT.time.orig);
    BPT.time.orig = BPT.time.orig./median(abs(BPT.time.orig(:)))/4;
    BPT.time.orig = BPT.time.orig-mean(BPT.time.orig);
    BPT.time.filt = zeros(size(BPT.time.orig));
    BPT.time.filt = lowpass(BPT.time.orig, BPT.info.lowpass_cutoff, BPT.info.fs);
    BPT.time.filt=BPT.time.filt-mean(BPT.time.filt);

    % plot results
    figure(1);
    t = tiledlayout(1,4);
    nexttile
    bpt_plot(BPT.time.t,BPT.time.orig,'BPT time course (raw data)');
    nexttile
    bpt_plot(BPT.time.t,BPT.time.filt,['BPT time course (low pass filtered with
    cutoff = ',num2str(BPT.info.lowpass_cutoff),' Hz)']);
    nexttile
    bpt_plot(BPT.time.t,BPT.time.orig-BPT.time.filt,'noise (difference between raw
    and filtered)');
    nexttile
    barh(mean(abs(BPT.time.filt))./std(BPT.time.orig-BPT.time.filt));title('SNR
    (mean(filtered)/std(noise))');set(gca,'Ydir','reverse');

    t.Padding = 'compact';
    t.TileSpacing = 'compact';
    title(t,raw,'interpreter','none');rtree

    %% save results
    if saveresults
        saveas(gcf,[resultdir,mid,'_',num2str(dataset),'_BPT.png']);
        save(      [resultdir,mid,'_',num2str(dataset),'_BPT.mat'],'BPT');
    end
```

Die approbierte gedruckte Originalversion dieser Diplomarbeit ist an der TU Wien Bibliothek verfügbar
The approved original version of this thesis is available in print at TU Wien Bibliothek.
TU WIEN Bibliothek Your knowledge hub

bpt_plot Matlab script

```matlab
function bpt_plot(t,bpt,raw)
plot(t,0.5*bpt+repmat([1:size(bpt,2)],size(bpt,1),1));%offset channels to display above each other
axis tight
ylim([0 size(bpt,2)+1]);
set(gca,'Ydir','reverse');
yticks(1:size(bpt,2));
title(raw,'interpreter','none');
xlabel('time (s)');
ylabel('coil channel');
end

```

Die approbierte gedruckte Originalversion dieser Diplomarbeit ist an der TU Wien Bibliothek verfügbar
The approved original version of this thesis is available in print at TU Wien Bibliothek.